CHEMISTRY OF MATERIALS
ARTICLE
pubs.acs.org/cm

Disclosing the Complex Structure of UiO-66 Metal Organic Framework: A Synergic Combination of Experiment and Theory

Loredana Valenzano,[†,§] Bartolomeo Civalleri,[†] Sachin Chavan,[†] Silvia Bordiga,[†] Merete H. Nilsen,[‡] Søren Jakobsen,[‡] Karl Petter Lillerud,[*,‡] and Carlo Lamberti[*,†]

[†]Department of Inorganic, Physical and Materials Chemistry, NIS Centre of Excellence, and INSTM Reference Center, University of Turin, Via P. Giuria 7, I-10125 Torino, Italy

[‡]inGAP Centre of Research-based Innovation, Department of Chemistry, University of Oslo, Sem Saerlandsvei 26, N-0315 Oslo, Norway

S *Supporting Information*

ABSTRACT: Through a combined use of experimental and theoretical approaches such as XRPD, EXAFS, IR, and UV—vis spectroscopies and ab initio periodic DFT calculations, we report a detailed characterization of structural, vibrational, and electronic properties of UiO-66 (Zr-BDC MOF) in its hydroxylated and dehydroxylated forms. The stability of the materials with respect to the most common solvents, acids, and bases is determined by combining XRPD and TGA/MS techniques. The structures of the two forms of UiO-66 are refined through an interactive XRPD/EXAFS approach and validated by ab initio calculations. Experimental and calculated IR spectra are reported and compared to enlighten the nature of vibrational modes upon dehydroxylation and to show the complete reversibility of the dehydration/hydration phenomenon. Experimental and calculated band gaps are also reported and compared. In this work, we show the necessity to combine, in a synergic way, different experimental techniques and periodic ab initio approaches to disclose and fully understand the nature of complex novel materials such as UiO-66 on structural, vibrational, and electronic grounds. The correct structure refinement could not be possible using one of these three approaches alone, in particular, XRPD data were unable to detect an important distortion of the Zr_6O_6 units of the dehydrated material that was, however, foreseen in the ab initio calculations and measured in the EXAFS spectra.

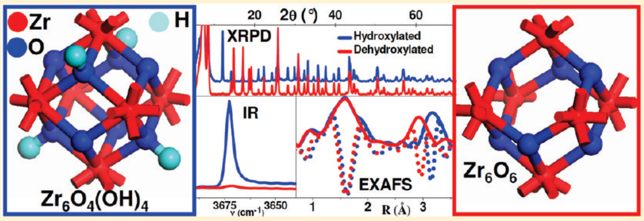

KEYWORDS: MOF, structure refinement, XRPD, EXAFS, microporous materials, ab initio modeling, short range order, long range order

1. INTRODUCTION

Microporous (and nanoporous) materials have proven to be highly valuable materials for industrial applications within petrochemistry, catalysis, and selective separation.[1] Their unique property is based on the molecular scale porous character. Metal organic frameworks (MOFs) provide us with a new world of possibilities in the design of both geometrical shape and chemical properties of the internal surface of nanoporous materials. MOFs are built up from inorganic bricks and organic complexing molecules acting as spacers, creating open porous three-dimensional structures, with very high pore volumes and surface areas. This hybrid architecture opens the possibility to design and synthesize a great variety of new porous materials, which are in principle able to display novel functionalities, potentially exploitable for a number of applications in catalysis, ion-exchange, non linear optics, as sensors, in gas separation, and/or storage.[2−31]

In the synthesis of new MOFs, the structure of the organic linkers can be controlled; on the other hand, the formation of the inorganic building brick and its coordination with the organic linkers is still pure serendipity. However, once the synthesis of an inorganic brick is established, it is possible to reproduce it also in combination with new linkers. This has been demonstrated both by the elegant isoreticular synthesis of the IRMOF-1-16[32] and by the fact that an impressive number of new MOFs are based on surprisingly few highly symmetrical inorganic building units. Some representative examples are the $Cu_2(OH)_2(CO_2)_4$ brick from HKUST-1,[33] the $Zn_4O(CO_2)_6$ brick from MOF-5,[34] and the $Cr_3O(OH)_3(CO_2)_6$ cornerstone from MIL-88.[35]

Here, we present a detailed characterization of UiO-66, a recently discovered MOF for which the cornerstone is based on a $Zr_6O_4(OH)_4$ octahedron,[36−38] forming lattices by 12-fold connection through a 1,4-benzene-dicarboxylate (BDC) linker[39] (Figure 1). Linker substitution with 4,4′ biphenyl-dicarboxylate (BPDC) or with terphenyl dicarboxylate (TPDC) leads to the formation of isoreticular UiO-67 and UiO-68 MOFs, respectively; this series of MOFs is characterized by a high surface area and by a linker independent, unprecedented stability.[39] We shall refer in the following to this class of materials as UiO-66/8.

Received: August 11, 2010
Revised: January 10, 2011
Published: March 04, 2011

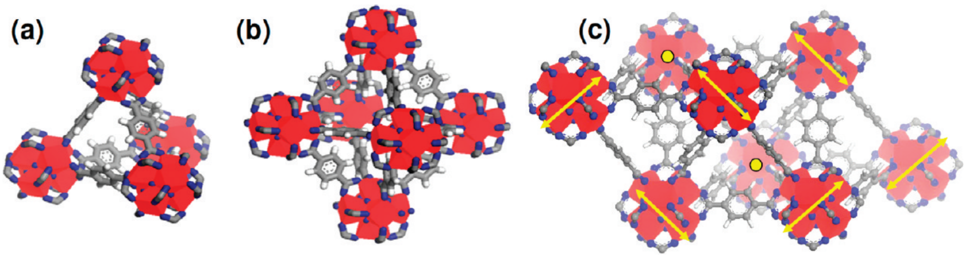

Figure 1. Structure of UiO-66 MOF. (a): Representation of a super tetrahedron cage. (b): Representation of a super octahedron cage. (c): Combination of one octahedral cage and two adjacent tetrahedral cages forming a cubic unit consisting of eight inorganic $Zr_6O_4(OH)_4$ bricks. Zirconium, oxygen, carbon, and hydrogen atoms are represented in red, blue, gray, and white, respectively. Yellow arrows indicate the squeezing direction that the Zr_6O_6 octahedron undergoes after the dehydroxylation process (Section 4.3). Yellow circles represent arrows pointing toward the reader. For each Zr_6O_6 octahedron, this direction randomly coincides with one out of its three diagonals.

Such a high stability is related to the fact that each Zr octahedron is 12-fold connected to adjacent octahedra. This connectivity is very common for metals, resulting in a highly packed fcc structure, but it is still almost unique in MOF topologies. To the best of our knowledge, only two other examples of 12-fold connected MOFs can be mentioned: the UiO-66 isostructural MOF synthesized using the *trans,trans* muconic acid as the ligand by the Ferey group,[40] and the aluminum-based CAU-1.[41] In this regard, it is worth noticing that an interesting review of known secondary building units (SBUs) has recently been published,[13] where the zirconium SBU recognized in this structure is listed as an 11 extension point cluster, while authors list 20 possible 12 extension point clusters.

In the Oslo group, MOFs with this topology have been synthesized with a large number of linkers, including pure carboxylates, tagged and functionalized.[42] This paper will focus on the zirconium brick and its prototype structure, UiO-66. Expanded versions of this MOF, UiO-67 and UiO-68, have already been synthesized,[39] while functionalized versions are in progress.[42] The formation and stability of (arene)$Cr(CO)_3$ species inside UiO-66 has recently been highlighted,[43] combining FT-IR, UV−vis, EXAFS and XANES spectroscopies, coupled with theoretical calculations. Covalent postsynthetic modifications of the UiO-66-NH_2 MOF (obtained using 2-amino-terephthalate ligand) with four different acid anhydrides have recently been demonstrated.[44] The same philosophy has inspired Garibay and Cohen, who have synthesized amino, bromo, nitro, and naphthalene functionalized UiO-66 through reticular chemistry, showing that UiO-66-NH_2 is suitable for postsynthetic modification with a variety of anhydrides to generate new functionalized frameworks.[45] The group at Valencia has shown that UiO-66 and UiO-66-NH_2 exhibit photocatalytic activity for hydrogen generation in methanol or water/methanol upon irradiation at wavelengths longer than 300 nm, representing good candidates for the development of more efficient MOF-based water-splitting materials.[46] Finally, grafted UiO-66 has shown a photoinduced reactivity substituting of one CO ligand with a N_2 molecule under UV irradiation.[43]

The high structural stability of the UiO-66/8 class of materials, able to resist in air up to 375 °C independently to the ligand, does not hold for thermal treatments only. In this work, we document the stability of UiO-66 in the most used solvents such as water, benzene, acetone, ethanol, and DMF; we also checked its resistance in the presence of a strong acid (HCl) and a strong base (NaOH). Such remarkable stability is a fundamental prerequisite to foresee practical applications of UiO-66 or of some of its functionalized forms discussed above.[42−46]

It is a matter of fact that the structural refinement of complex materials (with unit cells exhibiting volumes on the order of ten thousand $Å^3$) from powder XRD (XRPD) data is a difficult task. In the present case, Rietveld refinement of XRPD pattern desolvated UiO-66 could be obtained with satisfactory *R* factors using different models that predict significantly different Zr−O and Zr−Zr distances. To discriminate among the different structural models proposed by XRPD refinement, Zr K-edge EXAFS analysis and periodic ab initio calculations were performed. This is not the first time that a combined diffraction and EXAFS approach has been needed to fully clarify the structure of a complex material. In fact, when a local disorder is included within a periodic lattice, both long-range order (measured by diffraction methods) and local order (measured by EXAFS) are needed to have a global picture. This is the case of ternary $A_xB_{1-x}C$ (and quaternary $A_xB_{1-x}C_yD_{1-y}$) semiconductor alloys. Diffraction data are compatible with the virtual crystal approximation (VCA) predicting an isotropic cell expansion/contraction that is linear with the amount of A inclusion in the BC lattice: $a_{ABC}(x) = (x)a_{AB} + (1 - x)a_{BC}$. EXAFS evidence shows the distortion of the local geometry from the tetrahedral one finding R_{AC} and R_{BC} bond lengths much closer to those of the pure AC and BC binary compounds than foreseen from the VCA approximation.[47−52] Another example comes from mixed oxides with the brownmillerite $ABO_{2.5}$ structure; brownmillerite exhibits an alternation of BO_6 octahedra layers with BO_4 tetrahedra. While BO_6 octahedra do not show any preferred orientation, BO_4 tetrahedra do. Depending on the orientation of the BO_4 tetrahedra, the $ABO_{2.5}$ structure can belong to *Pnma*, *Imma*, or *I2mb* space groups.[53] The general problem lays in the fact that only slight differences exist in the arrangement of the BO_4 tetrahedral chains for these three space groups. *I2mb* and *Pnma* refer to two different ordering schemes for the BO_4 chains, while *Imma* implies a statistical disorder of BO_4 tetrahedra, which is approximately equivalent to a coherent mixing of *Pnma* and *I2mb* domains.[53] Note that also a dynamically disordered structure has recently been proposed in the $SrFeO_{2.5}$ case.[54]

In all cited cases, where local and long-range order behave differently, the combined use of diffraction and EXAFS techniques was determinant to understanding the material structures. Here, these two independent experimental approaches are further improved by a periodic ab initio DFT (at the B3LYP level of theory) computational study carried out by using the CRYSTAL code.[55,56] This methodology was already successfully applied to the study of other MOF materials such as MOF-5,[57] Cr-MIL-53,[58a] Al-MIL-53,[58b] and MOF-74-Mg.[59]

Results reported in this paper and the related discussion are structured into three separate sections. Section 3 is aimed to testify on the remarkable stability of UiO-66 framework. The complex procedure, requiring the combined use of XRPD, EXAFS, and ab initio calculation, adopted to solve the structure of both solvated and desolvated forms of the UiO-66 framework is described in detail in Section 4. Finally, Section 5 is devoted to analyze, on both experimental and theoretical grounds, the vibrational and electronic properties of UiO-66.

From this study it emerges that the thermal activation of UiO-66 proceeds in three successive steps: (i) dehydration (physisorbed water); (ii) solvent removal; (iii) dehydroxylation of the $Zr_6O_4(OH)_4$ cornerstone into Zr_6O_6.

2. EXPERIMENTAL AND METHODS

2.1. Material. All chemicals were obtained commercially (Aldrich) and used without further purification. Standard synthesis of Zr-BDC MOF was performed by dissolving $ZrCl_4$ (0.227 mmol) and 1,4-benzenedicarboxylic acid (H_2BDC) (0.227 mmol) in N,N′- dimethylformamide (DMF) (340 mmol) and H_2O (0.227 mmol) at room temperature. The obtained mixture was sealed and placed in a preheated oven at 120 °C for 24 h. Crystallization was carried out under static conditions.

The adsorption of nitrogen was measured volumetrically with a BELSORP-mini II instrument, and the specific surface area was obtained by the BET method. The sample was heated to 250 °C and kept at this temperature under continuous evacuation for 6 h prior to the adsorption measurement. The adsorption of nitrogen follows a type I isotherm with no hysteresis, and with a BET surface area of 1069 m^2/g (see Figure S1 in the Supporting Information).

2.2. Characterization. XRPD data on as-prepared and desolvated UiO-66 were collected in transmission mode with a Siemens D5000 diffractometer using Cu $K_{\alpha 1}$ radiation, selected from the incident beam with a Ge monochromator. The detector was a Braun PSD. The sample was kept in a rotating 0.5 mm quartz capillary. The diffraction patterns were collected for 24 h each in the 3−100° 2θ range. Extractions of the peak positions, pattern indexing, and Rietveld refinements[60,61] were carried out with the TOPAS program.[62,63] In the process of solving the structures from XRPD, several lower symmetries that also index with a very acceptable figure of merit (tetragonal, orthorhombic, and monoclinic) were considered and structure solution with EXPO were performed in all reasonable unit cells. Nevertheless, nearly all of them had to be excluded due to the mismatch between the Zr−O and Zr−Zr distances that there were known from EXAFS within few hundred angstroms. (Section 4.2.1).

Temperature-resolved XRPD data were recorded on a Siemens D500 instrument equipped with Cu X-ray tube combined with a β filter. The experiment was performed in a Bühler furnace, allowing customized temperature programming and atmosphere control. The sample was smeared on a Pt filament, and data were collected in the 5−35° 2θ range in steps of 25 °C in the temperature range of 25−450 °C in air flow.

Thermogravimetric analysis (TGA) and temperature-controlled adsorption/desorption (TPA/TPD) were carried out in a Rheometric Scientific STA1500 instrument. Around 10 mg was placed in an Al_2O_3 crucible. The TGA profile of the sample was obtained by heating it from ambient temperature to 950 °C (heating rate 2 °C/min with continuous N_2 flow). The instrument is equipped with a quadrupole mass spectrometer (MS) to investigate the chemical nature of the species leaving the sample in the TGA run.

The FTIR spectra were recorded in controlled atmosphere at 2 cm^{-1} resolution on a Bruker IFS 66 FTIR spectrophotometer, equipped with a MCT and DTGS detectors. The FTIR spectra were collected in transmission mode on a thin film of the UiO-66 sample, prepared by deposition of Zr-MOF- water suspension on a silicon wafer. DRS-UV−vis-NIR measurements were performed on a Varian Cary 5000 spectrometer equipped with a reflectance sphere on thick self-supported pellets.

X-ray absorption experiments on Zr K-edge were performed at the BM29 beamline[64] at the European Synchrotron Radiation Facility (ESRF). The monochromator was equipped with two Si(111) flat crystals, and harmonic rejection was achieved using Rh-coated mirrors after monochromator. The following experimental geometry was adopted: (1) I_0 (10% efficiency), (2) MOF sample, (3) I_1 (50% efficiency), (4) reference Zr foil, and (5) I_2 (80% efficiency). This setup allows a direct energy/angle calibration for each spectrum avoiding any problem related to energy shifts due to small thermal instability of the monochromator crystals.[65a] For the XANES part, a sampling step of 0.5 eV was applied, while for EXAFS part, a sampling step of 0.05 $Å^{-1}$ was considered with an integration time of 3 s/point. Samples, in the form of self-supported pellets of optimized thickness, were located inside an ad hoc conceived cell.[65b] The extraction of the $\chi(k)$ function was performed using the Athena code.[66] For each sample, three consecutive EXAFS spectra were collected, and corresponding $\chi(k)$ functions were averaged before data analysis. EXAFS data analysis was performed using the Arthemis software.[66] phase, and amplitudes for all single scattering (SS) and multiple scattering (MS) paths were calculated by FEFF6 code[67] using as input the structure solved by powder X-ray powder diffraction. For the as-prepared sample, the averaged $k^3\ \chi(k)$ function were Fourier transformed in the Δk = 2.00−18.00 $Å^{-1}$ interval. The fits were performed in R-space in the ΔR = 1.00−5.30 Å range ($2\Delta k\Delta R/\pi > 43$). For the desolvated sample, values were Δk = 2.00−15.00 $Å^{-1}$; ΔR = 1.00−5.30 Å; and $2\Delta k\Delta R/\pi > 35$.

2.3. Theoretical Methods. The theoretical investigation of UiO-66 Zr-MOF (in its hydroxylated and dehydroxylated structures) was carried out with periodic density functional theory (DFT) calculations employing the hybrid B3LYP[68,69] functional as implemented in the CRYSTAL program.[55,56] Crystalline orbitals (CO) are represented as linear combinations of Bloch functions (BF) and are evaluated over a regular three-dimensional mesh in the reciprocal space. Each BF is built from local atomic orbitals (AO), which are contractions (linear combinations with constant coefficients) of Gaussian-type functions (GTFs), each GTF being the product of a Gaussian times a real solid spherical harmonic.

All electron basis sets were used for Zr, O, C, and H atoms; they consist of (8s)−(7631sp)−(621d), (8s)−(411sp)−(1d), (6s)−(31sp)−(1d), and (31s)−(1p), respectively. Basis sets for Zr and O were taken from refs 70 and 71, whereas for C and H standard 6-311G(d,p), basis sets from Pople's family were adopted. Polarization functions (one shell) were used on H, C, and O atoms. The corresponding exponents are $\alpha(H, p)$ = 0.1; $\alpha(O, d)$ = 0.8, and $\alpha(C, d)$ = 0.8. For Zr, an extra d-function was adopted with exponent $\alpha(Zr, d)$ = 0.4. The effect of a polarization f orbital (α = 0.6) was investigated showing no significant improvement in the results.

For the numerical integration of the exchange-correlation term, 75 radial points and 974 angular points (XLGRID) in a Lebedev scheme in the region of chemical interest were adopted. The condition for the SCF convergence was set to 10^{-8} and 10^{-10} Hartrees during geometry optimization and frequency calculation steps, respectively. The Pack−Monkhorst/Gilat shrinking factors for the reciprocal space were set to 2, corresponding to 3 real reciprocal space points at which the Hamiltonian matrix was diagonalized. The five truncation criteria (TOLINTEG) for the bielectronic integrals (Coulomb and HF exchange series) were set to 7 7 7 7 16.[55] A modified Broyden scheme[72] following the method proposed by Johnson[73] was adopted to accelerate convergence in the self-consistent calculations; the method was applied after five SCF iterations, with 50% of Fock/KS matrices mixing and with the Johnson parameter set to 0.05. The above computational parameters ensured a full numerical convergence on all the computed properties described in this work.

Both the hydroxylated and dehydroxylated structures were derived from the experimental geometry (cubic, space group $Fm\bar{3}m$, No. 225); the

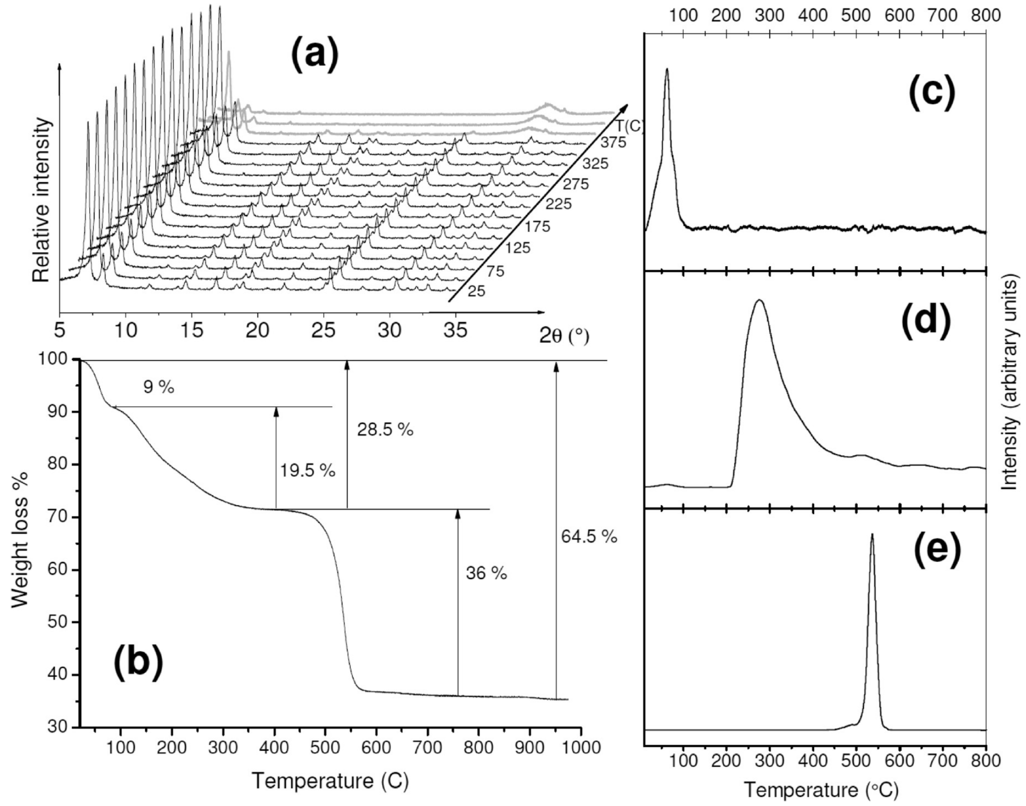

Figure 2. (a): Evolution of XRPD pattern profiles of UiO-66 upon increasing activation temperature in air. (b): TGA curve of UiO-66 in air flux. (c), (d), (e): MS signals of water, DMF, and benzene along the TGA experiment reported in panel (b).

former was optimized in the space group $F\bar{4}3m$ (cubic, No. 216), while the calculations on the latter were performed in the space group $R\bar{3}$ (trigonal, No. 148). A full relaxation of the structures (both lattice parameters and atomic positions) was performed by keeping the symmetry of the systems; optimizations were iterated until no changes appeared in the geometry. The calculations of vibrational frequencies at the Γ point, were performed on the optimized geometry by means of a mass-weighed Hessian matrix obtained by numerical differentiation of the analytical first derivatives.[74−76] Full details and discussion of the computational conditions and other numerical aspects can be found elsewhere.[77]

3. REMARKABLE STRUCTURE STABILITY

As briefly mentioned in the communication highlighting the synthesis and the structure of the new class of MOFs materials,[39] UiO-66, UiO-67, and UiO-68 are extremely stable upon thermal treatments and are able to maintain their crystallinity upon interaction among some rather aggressive chemical solvents. These are two characteristics of this new class of materials of particular relevance because such a remarkable resistance opens a large number of potential applications, particularly in the field of catalysis. For this reason, it is worth discussing the stability property of UiO-66 in more detail.

3.1. Structure Stability upon Thermal Treatment. Temperature-dependent XRPD investigation indicates that the UiO-66 framework is stable in air up to 375 °C (Figure 2a). No changes of the XRPD pattern are appreciable until structure collapse. We performed a parallel TGA/MS experiment in order to (i) confirm XRPD results, (ii) learn about the temperature needed to remove the solvent, and (iii) understand the chemical nature of the fragments formed upon framework collapse. The TGA curve reported in panel (b) of Figure 2 exhibits a progressive structured weight loss up to 300 °C, with a clear shoulder around 100 °C. MS spectroscopy, panels (c) and (d) of Figure 2, shows that the sample is loosing physisorbed water first and DMF molecules afterward. In the 300−500 °C interval, a stability plateau at 71.5% of the starting weight is observed. In the successive 50 °C, there is a significant weight loss, and the sample is left with the 35.5% of the starting weight. XRPD testifies the crystallinity up to 375 °C, with subsequent amorphization of the structure and pore collapse. Loss of benzene fragments starts around 500 °C and is over already at 550 °C. The residual material at the end of the TGA experiment is simply ZrO_2, with a very low degree of crystallinity.

3.2. Effect of Structure Defectivity (Linker Vacancy) in the Thermal Stability. Summarizing the results reported in Figure 2, the sample loses 9 wt % of water, 19.5 wt % of solvent, and 36 wt % of benzene. Both physisorbed water molecules and solvent molecules hosted in the pores cannot be exactly defined stoichiometrically, but the loss of benzene ring can. The dehydrated and desolvated material, corresponding to the plateau in the 300−500 °C range in the TGA curve, refers to a chemical formula per Zr atom of $ZrO(CO_2)_2(C_6H_4)$. Assuming that the final residual at high temperature is ZrO_2, we expect a weight loss, relative to this last step, of 54.6%. The experimental datum exhibits a relative weight loss (from 71.5 to 35.5 wt %) of only 50%. As we cannot expect to have BDC ligands still anchored to the Zr units at such a high temperature, we must hypothesize that such ligands were missing in the starting structure. This means that the as-synthesized material is slightly defective, exhibiting about 11 ligands per inorganic $Zr_6O_4(OH)_4$ cluster. As the absence of 1/12 of the BDC ligands is supposed to occur randomly in the framework, we could not hope to detect it by crystallographic methods.

The presence of defects implies the lack of negatively charged linkers that has to be somehow compensated to ensure the charge neutrality of the structure. Of course, $(OH)^-$ groups may saturate the dangling bonds of the positively charged inorganic clusters. Note that a minor fraction of OH groups is still present after desolvation (see the red curve in the inset of Figure 4b). An alternative explanation is related to the fact that DMF coordinates to Zr during the formation of MOF. Some of the DMF molecules react with the $ZrCl_4$ precursor during the initial mixing as a release of HCl gas is observed. This happens also when very dry DMF is used in the synthesis. A zirconium DMF adduct is formed in this stage of the synthesis, and a minor fraction of this very strongly coordinated DMF may not have been exchanged with a BDC linker, being still coordinated to Zr at the end of the process.

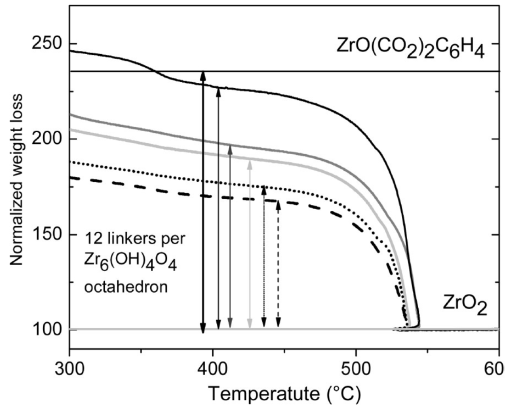

Figure 3. High-temperature part of the TGA curves of UiO-66 samples synthesized in different batches. For all curves, the ordinate axis was normalized to 100 for the solid residual at high temperature, corresponding to ZrO_2, gray horizontal line. In this scale, the dehydrated, desolvated UiO-66 should have a stoichiometry of $ZrO(CO_2)_2(C_6H_4)$, corresponding to a normalized weight of 235.7 (black horizontal line). The horizontal bold arrow represents the expected weight loss for an ideal UiO-66 material characterized by 12 BDC linkers per $Zr_6O_4(OH)_4$ octahedron. Experimental curves, reporting a lower weight loss (see vertical arrows with the same line code) at this stage testify of the presence of framework defectivity: linker vacancies.

The absence of some linkers connecting the inorganic cornerstones is further confirmed by the comparison of the last part of the TGA curves collected on samples synthesized in different batches (Figure 3). In the other batches (reported as gray, dotted, and dashed curves), the relative weight loss of this last step is even smaller, down to 26 wt % (dashed curve), compared to the 54.6% of the stoichiometrically perfect framework. In this last case, about half of the benzene ligands are missing in the as-prepared material. Several intermediate cases were observed. It is worth noting that the fraction of framework defectivity, clearly evidenced by the height of the 300−500 °C plateau in the TGA curves (evidenced in Figure 3 by the vertical arrows drawn in the same line code as the corresponding experimental curves), correlates with a progressive decrease of the fragmentation temperature. The high thermal stability of UiO-66 was claimed because of the fact that the inorganic unit is 12-coordinated,[39] the highest coordination reported for a MOF, corresponding to the coordination of metal atoms in closed packed metal structures. In the set of experiments reported above, it is clearly evidenced that the stability is compromised when the density of defects increases. On the other hand, it is evident that further stability improvement can be foreseen when an almost defect-free UiO-66 material could be synthesized. In the remaining part of this work, all measurements refer to the less defective material.

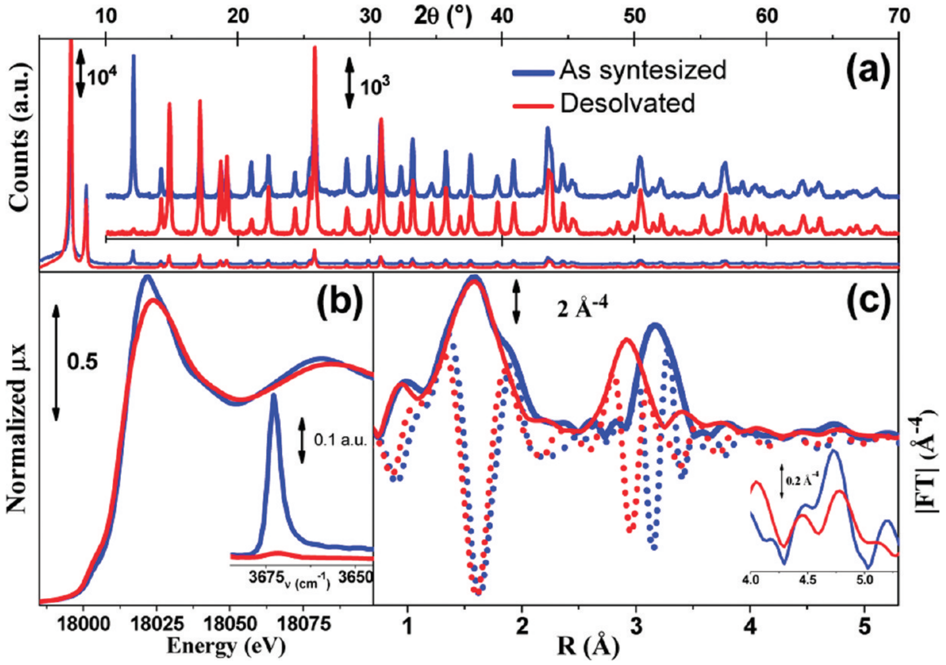

Figure 4. Effect of desolvation on UiO-66 observed with different techniques: blue curves refer to the as-prepared material, red curves to the desolvated one. (a): XRPD data collected with $\lambda = 1.5406$ Å. Inset reports a magnification on the high 2θ region. (b): XANES data. Inset reports the IR spectrum in the O−H stretching region. (c): k^3-weighted, phase uncorrected, FT of EXAFS. Full and dotted curves refer to moduli and imaginary parts, respectively. Inset reports a magnification of the high *R*-region, where the Zr−Zr contributions from the three diagonal of the Zr_6 octahedron are expected.

3.3. Structure Stability upon Interaction with Solvents and Chemicals. In the perspective to use UiO-66 as support for a catalyst, or a functionalized version of UiO-66 as catalyst or photocatalyst itself,[43] once the thermal stability was carefully checked,[39] the stability of the material in the presence of the most used solvents has to be verified. XRPD studies (Figure S2 of the Supporting Information) indicate that the UiO-66 framework is stable in water, benzene, acetone, ethanol, and, obviously, DMF. As some reactions run at pH values significantly different from neutrality, we also checked the stability in the presence of a strong acid (HCl) and a strong base (NaOH). The patterns reported in Figure S2 of the Supporting Information indicate that UiO-66 is well stable in a HCl solution and that it still maintains an appreciable degree of crystallinity in NaOH solution. Summarizing, UiO-66 is a highly interesting material of potential applied interests. The next sections are devoted to a deeper understanding of its structure, for both as-synthesized and desolvated forms, by means of different experimental and theoretical approaches.

4. XRPD, EXAFS, IR, AND AB INITIO COMBINED STRUCTURE REFINEMENT

Solving complex structures with powder data, even if of high quality, is far from trivial.[78−82] In the present case, several possible models were tried. For each case, the most relevant Zr−O and Zr−Zr distances were checked with those independently obtained via EXAFS spectroscopy. Those where the agreement was not satisfactory were rejected and a new model was tried to refine XRPD data. First, raw experimental data will just be described and compared (Section 4.1), then the complex refining procedure, requiring an interactive progressive optimization of XRPD and EXAFS data, will be described in detail for the hydroxylated material (Section 4.2) and then applied straightforwardly for the dehydroxylated form in Section 4.3.

4.1. Effect of Solvent Removal: Comparison between XRPD, EXAFS, and IR Raw Data. Comparison of the XRPD data collected on the as-prepared material (blue) and after solvent removal at 300 °C (red) is reported in panel (a) of Figure 4. Only minor changes in the powder pattern are caused by the heat treatment (Figure 2a). Upon solvent removal, the unit cell is nearly unchanged, moving from a = 20.7551(5) to 20.7004(2) Å. Regarding the intensities of the reflections, the line at 12.0° (d = 3.70 Å) nearly disappears, while the rest of the pattern remains virtually unaffected by the solvent removal. It is probably the presence of the diagonal linkers combined with the strong linker−inorganic brick interaction that is responsible for this high rigidity of the UiO-66 structure.[39]

The solvent removal effect, leaving the XRPD patterns almost unaffected (Figure 4a), has a non-negligible effect on the XANES spectra (Figure 4b) and surprisingly an important effect on the EXAFS spectra (Figure 4c). In particular, the intensity decrease of the white line (first resonance after the edge) suggests a loss of ligands in the first coordination shell around Zr. Coming to the EXAFS part, a small contraction of the first shell distance (due to Zr−O SS), better appreciated in the imaginary parts (also a small decrease in the coordination is evidenced by the erosion of the shoulder around 1.9 Å), and a dramatic distortion of the second shell contribution (due to Zr−Zr SS, which maximum moves from 3.17 Å to 2.91 Å, with a shoulder at 3.41 Å) are clearly observed. Finally, the weak contribution around 4.7 Å (due to the Zr−Zr SS signal of the octahedron diagonal, better visible in the inset) is distorted and significantly weakened in intensity because of heterogeneity effects. This important different evolution of XRPD patterns and EXAFS spectra upon solvent removal is striking and implies that the material evolves differently on local and long-range levels. Consequently, the final models for both structures must be able to explain both XRPD and EXAFS evidence. Once such agreement among experimental data was obtained, and the final models were used as input for periodic ab initio calculation to further verify the validity of the structures.

Of high relevance for the structural determination are the details of the IR spectra reported in the inset of panel (b) of Figure 4 showing that the desolvation process fully removes the huge absorption at 3673 cm^{-1} due to well-defined OH groups.[83−85] This important experimental evidence must be considered when the models of the as-prepared and desolvated materials are put forward. On the basis of the results reported in the inset of panel (b) of Figure 4, we shall refer in the following to hydroxylated and dehydroxylated forms of UiO-66 material.

4.2. As-Synthesized Material: XRPD, EXAFS, and ab initio Combined Structure Refinement. *4.2.1. As-Prepared Material: Preliminary Determination of the Main Signals in the EXAFS spectrum.* Independently from any accurate 3-D structure coming from XRPD refinement or ab initio calculation, EXAFS is able to give little, but well-defined, information concerning the local environment around Zr atoms in terms of bond distances (R), thermal factors (or Debye−Waller factors σ^2), and coordination numbers (N). Actually, without any structural model, EXAFS provides an estimation of the product $N\cdot S_0^2$, the latter being the amplitude factor;[48,86] however, being usually S_0^2 close to unit, the estimated product can be considered in first approximation close to the coordination number. On a chemical ground, the two peaks dominating the EXAFS spectrum in the 1−2 Å and in the 2.9−3.6 Å regions must be mainly due to Zr−O and Zr−Zr SS contributions (blue curve in Figure 4b). A first attempt to model the first shell peak using a single Zr−O SS path, resulted in a satisfactory agreement between experimental and theoretical curves (R-factor of 3.8%, see first fit in Table 1). However, the estimated N and σ^2 values were out of the expected range (Table 1). Zirconium atoms should be 12-fold coordinated with a Debye−Waller (σ^2 = 0.014 Å^2, σ = 0.12 Å) almost five times larger than that expected from a pure thermal vibration of a Zr−O bond in a highly crystalline material, where structural disorder due to heterogeneity may not be invoked. These are clear indications that the first peak in the EXAFS spectrum (1−2 Å) is due to the overlap of two, significantly different, Zr−O bonds. The fit of the first shell contribution with two independent Zr−O shells improves significantly (R-factor of 1.6%, see second fit in Table 1) and, most importantly, obtained N and σ^2 values lay in chemically and physically acceptable ranges. Thus Zr atoms result to be 8-fold coordinated with two short (2.09 Å) and six long (2.23 Å) Zr−O bonds. The fact that the addition of a second Zr−O path is necessary to correctly model the first shell of the experimental datum is testified by the important decrease in the error bars associated to all optimized parameters and by a decrease in the correlation among parameters (that, conversely, increases when an irrelevant parameter is included in the fit). A fit over a larger R-interval fully confirms this picture (see third fit in Table 1), the second shell peak being due to a unique, 4-fold degenerated, Zr−Zr contribution around 3.51 Å.

4.2.2. As-Prepared Material: XRPD Refinement. The UiO-66 structure was solved first for its desolvated form using Fm-3m space group (No. 225),[39] resulting in excellent profile factors: R_P = 0.016 and R_{WP} = 0.022 (Section 4.3). This choice was dictated by the need to remove the huge electron density of the

Table 1. Summary of Preliminary Attempts to Single Out the Main Signals Contributing to the overall EXAFS Spectrum of UiO-66 in Its Hydroxylated Form[a]

shell	*R*-range	N_I/N_v	$N\cdot S_0^2$	ΔE_0 (eV)	*R* (Å)	σ^2 (Å^2)	*R*-factor	highest correlations
Fit of the first shell peak with a single Zr−O contribution								
Zr−O	1.0−2.2	11.8/4	11.4 ± 2.4	5 ± 1	2.20 ± 0.02	0.014 ± 0.003	0.038	$N\cdot S_0^2/\sigma^2 = 0.92$
								$\Delta E_0/R_{\text{Zr}-\text{O}} = 0.84$
								$N\cdot S_0^2/\Delta E_0 = -0.40$
								$\lvert\text{remaining}\rvert < 0.25$
Fit of the first shell peak with two independent Zr−O contributions (with common ΔE_0 and S_0^2)								
Zr−$O_{\mu 3}$	1.0−2.2	11.8/6	2.4 ± 0.3	5 ± 1	2.09 ± 0.01	0.005 ± 0.001	0.016	$\Delta E_0/R_{\text{Zr}-\text{O}} = 0.82$
Zr−O			7.2 ± 1.0		2.23 ± 0.01	0.008 ± 0.001		$\sigma^2(\mu_3-\text{O})/\sigma^2(\text{O}) = 0.77$
								$\Delta E_0/R\mu_{3-\text{O}} = 0.76$
								$N\cdot S_0^2/\sigma^2(\mu_3-\text{O}) = 0.71$
								$\lvert\text{remaining}\rvert < 0.70$
Fit of the first 2 peaks with 2 Zr−O contributions and a single Zr−Zr contribution (with common ΔE_0 and S_0^2)								
Zr−$O_{\mu 3}$	1.0−3.6	26.2/8	2.0 ± 0.1	6 ± 1	2.09 ± 0.01	0.004 ± 0.001	0.057	$\Delta E_0/R_{\text{Zr}-\text{Zr}} = 0.80$
Zr−O			6.0 ± 0.4		2.232 ± 0.009	0.007 ± 0.001		$\Delta E_0/R_{\text{Zr}-\text{O}} = 0.68$
Zr−Zr			4.0 ± 0.3		3.515 ± 0.007	0.0068 ± 0.0006		$N\cdot S_0^2/\sigma^2(\mu_3-\text{O}) = 0.61$
								$\sigma^2(\mu_3-\text{O})/\sigma^2(\text{O}) = 0.60$
								$\lvert\text{remaining}\rvert < 0.50$

[a] In all cases $\Delta k = 2.0-18.0$ Å^{-1}. $N_I = 2\Delta k\Delta k/\pi$ is the number of the independent degree of freedom, and N_v is the number of variables optimized in the fit.

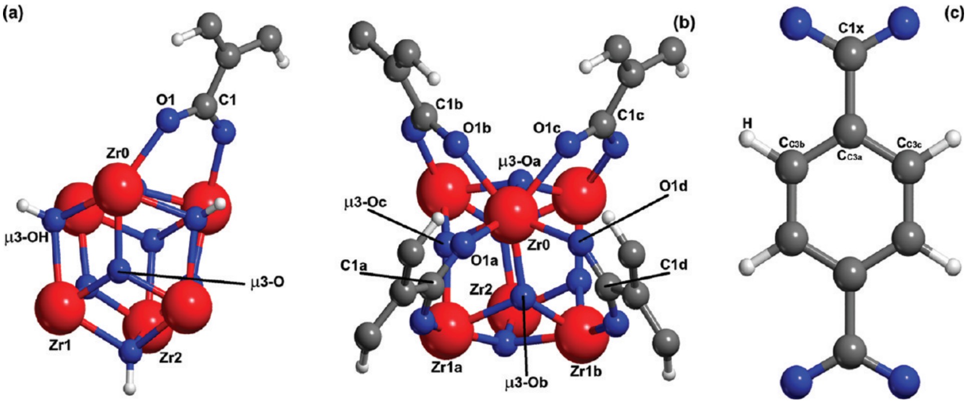

Figure 5. Structures show the inner core Zr_6 clusters drawn with the irreducible part of the organic linkers in their hydroxylated (a) and dehydroxylated (b) forms with respect to the (001) orientation. Zirconium, oxygen, carbon, and hydrogen atoms are red, blue, gray, and white, respectively. Atomic labels refer to distances reported in Tables 2− 5, being Zr0 the absorbing atom in the EXAFS data. (c): The organic linker is reported, and atomic labels refer to density of states (DOS) representation as in panels (b,c) of Figure 11.

DMF amorphous phase hosted inside the large pores. Because of the small differences in the XRPD patterns of the two phases of the material (Figure 4a), also the as-synthesized structure was refined in the *Fm*-3*m* space group (see Figure 7a for the final result). Extractions of the peak positions, pattern indexing, and Rietveld refinements were carried out with the TOPAS program.[62,63] The R_P and R_{WP} parameters, defining the fit quality, were of lower quality, reflecting the difficulty of the model to predict the peak intensities (while the peak position was correctly reproduced), that in turns reflect the difficulty of the model to simulate the charge density of the as prepared material. In the present case, this is not unexpected because the model contains only the framework-ordered atoms, neglecting the disordered atoms of the solvent filling the MOF pores. The framework atoms account for 1440 electrons per unit cell, while 3232 electrons are those of the DMF molecules; this means that the majority of the electron density is not ordered and explains the poorer *R* factors obtained in the Rietveld refinement of the as-prepared material. This statement, fully justifying the failure of the XRPD refinement in the quantitative reproduction of the peak intensities, does not represent a proof of validity for the framework model. Nevertheless, Zr−O and Zr−Zr bond distances are compatible with those obtained from the first preliminary EXAFS data analysis (Table 1).

The structure solution in space group $Fm\bar{3}m$ reveals an inner Zr_6O_8 core in which the eight triangular faces of the Zr_6 octahedron are capped by eight μ_3−O groups. Charge balancing requires the presence of four OH groups (observed by IR, see inset of Figure 4b), so that the Zr_6O_8 cluster should be a $Zr_6O_4(OH)_4$ as illustrated in panel (a) of Figure 5. We expect that four μ_3−O and four μ_3−OH groups are ordered within the cluster to minimize the electrostatic repulsion, changing the

Table 2. Summary of the EXAFS Refinement Obtained on the Hydroxylated (Δk = 2.0−18.0 Å^{-1}; ΔR = 1.0−5.3 Å) and Dehydroxylated (Δk = 2.0−15.0 Å^{-1}; ΔR = 1.0−5.3 Å, discussed below in Section 4.3) Forms of UiO-66[a]

	hydroxylated	dehydroxylated
R-factor	0.01	0.02
independent points	43	35
number of variables	14	14
ΔE_0 (eV)	5 ± 1.0	5
$S_0{}^2$	1.17 ± 0.08	1.17
$R_{\mu3-\mathrm{O}}$ (Å)	2.087 ± 0.008 (N = 2)	2.06 ± 0.01 (N = 2)
$\sigma^2(\mu_3-\mathrm{O})$ (Å^2)	0.0036 ± 0.0009 (N = 2)	0.008 ± 0.003 (N = 2)
R_{O1} (Å)	2.235 ± 0.008 (N = 6)	2.221 ± 0.007 (N = 5)
σ^2(O1) (Å^2)	0.0074 ± 0.0008 (N = 6)	0.007 ± 0.002 (N = 5)
R_{C} (Å)	3.19 ± 0.02 (N = 4)	3.17 ± 0.04 (N = 4)
σ^2(C) (Å^2)	0.004 ± 0.002 (N = 4)	0.009 ± 0.009 (N = 4)
R_{Zr1} (Å)	3.511 ± 0.007 (N = 4)	3.35 ± 0.01 (N = 8/3)
σ^2(Zr1) (Å^2)	0.007 ± 0.001 (N = 4)	0.009 ± 0.001 (N = 8/3)
R_{Zr1b} (Å)	−	3.74 ± 0.02 (N = 4/3)
σ^2(Zr1b) (Å^2)	−	0.009 ± 0.002 (N = 4/3)
R_{Zr2a} (Å)	4.99 ± 0.04 (N = 1)	4.14 ± 0.07 (N = 1/3)
σ^2(Zr2a) (Å^2)	0.010 ± 0.006 (N = 1)	0.008 ± 0.006 (N = 1/3)
R_{Zr2b} (Å)	−	5.30 ± 0.04 (N = 2/3)
σ^2(Zr2b) (Å^2)	−	0.008 (N = 2/3)
α	0.01 ± 0.01	0.00 ± 0.01
σ^2 (global) (Å^2)	0.004 ± 0.004	0.007 ± 0.003
highest correlations	$\Delta E_0/R_{\mathrm{O}}$ = 0.74	$\sigma^2(\mu_3-\mathrm{O})/\sigma^2(\mathrm{O})$ = 0.78
	$\sigma^2(\mu_3-\mathrm{O})/\sigma^2(\mathrm{O})$ = 0.69	$\sigma^2(\mathrm{O})/R_{\mu3-\mathrm{O}}$ = 0.76
	α/R_{Zr} = 0.65	$R_{\mathrm{O}}/\ \sigma^2(\mu_3-\mathrm{O})$ = −0.63
	|remaining| < 0.60	|remaining| < 0.56

[a] EXAFS refinement was obtained using as input model the optimized structure from XRPD and from ab initio calculations for the hydroxylated and dehydroxylated forms, respectively. With this approach the coordination number (N) of each contribution is fixed by the model stoichiometry; such values are reported for each shell in parentheses. Refinement of the experimental amplitude is done by optimizing the overall amplitude factor $S_0{}^2$ only. For the dehydroxylated form, the fitting of the higher shells was possible only by adopting the axial compressed model of the Zr_6O_6 octahedron represented in panel (c) of Figure 8, where twelve octahedron sides R_{Zr1} are split into eight short prismatic distances (R_{Zr1a}, N = 8/3) and four long planar ones (R_{Zr1b}, N = 4/3) and where the three diagonals R_{Zr2} are split into a short axial diagonal and (R_{Zr2a}, involving two Zr atoms out of six; N = 1/3) and two long planar diagonals (R_{Zr2b}, involving four Zr atoms out of six; N = 2/3). The quality of the fits can be appreciated looking to Figures 6 and 9 for the hydroxylated and dehydroxylated forms of UiO-66, respectively.

symmetry to T_{d} (−43 m). If all the clusters in the structure have the same orientation, a reduction of the symmetry to *F*-43*m* (No. 216) would be expected. However, the separation imposed by the long linkers should switch off the dipole interaction among OH groups belonging to neighbor clusters, resulting in a random arrangement. Under this hypothesis, the local order of the clusters is lost in the long-range scale, and XRPD will report an average position for the oxygen of four μ_3−O and four μ_3−OH groups, with a thermal parameter increased by site splitting (see Figure S3 in the Supporting Information). This site splitting is well observed by EXAFS and finds two different first shell distances separated by more than 0.1 Å (Table 1).[87] The successive sections are aimed to support the *Fm*-3*m* structure with independent experimental and theoretical approaches.

4.2.3. As-Prepared Material: Final EXAFS Refinement, using the Fm$\bar{3}$m XRPD Model.

The structural complexity of MOF materials implies that the overall EXAFS signal is the sum of a huge number of SS and MS contributions that can be fully considered only when a 3-D structure (obtained either from XRPD refinement or from ab initio modeling) is used as input for the calculation of all paths.[88−94]

The 3-D structure obtained from the Rietveld refinement in the *Fm*-3*m* space group of the hydroxylated material was used as input for a full EXAFS data analysis, performed on all SS and MS paths having a relative intensity (I_{r}) higher than 10% of that of the first Zr−O SS path and having a half path length (Reff) shorter than 5.3 Å.[95] The refinement was done by optimizing the amplitude factor $S_0{}^2$ and energy shift ΔE_0 (common to all paths), the bond distance, and the corresponding Debye−Waller factor for the two first shell Zr−O SS contributions [$R_{\mu3-\mathrm{O}}$, $\sigma^2(\mu_3-\mathrm{O})$, R_{O}, and σ^2(O), 2- and 6-fold degenerated merging, and the remaining two O atoms of the μ_3−OH groups and the four O atoms of the carboxylate units], for the 6-fold degenerated Zr−C SS path [R_{C} and σ^2(C)], for the 4-fold degenerated Zr−Zr SS path along the octahedral edges [R_{Zr1} (Å) and σ^2(Zr1)], and for the single Zr−Zr SS path along the octahedral diagonal [R_{Zr2} and σ^2(Zr2)], while for all remaining SS and MS paths, a unique Debye−Waller factor (σ^2, scaled with the square root of Reff.) and distance enlargement factor (α, parametrizing the path length variation as ΔR = α Reff.) was optimized, resulting in 14 free parameters.

The output of the XRPD refinement resulted technically in a high-quality fit of the EXAFS data (Table 2), characterized by a low *R*-factor, low correlation among optimized parameters, and physically meaningful Debye−Waller factors, ΔE_0 and $S_0{}^2$ parameters. Results reported in Table 2 also prove that the as-synthesized structure obtained from XRPD refinement in the *Fm*-3*m* space group is fully compatible with EXAFS data. A perfect agreement was found between the structure and distances optimized from XRPD and EXAFS, proving that, in spite of the high *R* factors, the XRPD refinement of the framework atoms was correct. Comparing XRPD and EXAFS refinements, we note that the two first shell Zr−O distances $R_{\mu3-\mathrm{O}}$ and R_{O1} agree within 0.03 Å.

Because of the different symmetries adopted in the two approaches, μ_3−O and O1 atoms have a different degeneration in the two approaches. So the corresponding distance should not be directly compared, but a comparison should be made on the averaged distances, where the disagreement between the two approaches becomes as small as 0.006 Å (Table 3). The cube edge (R_{Zr1}) agrees within 0.02 Å, while the almost perfect agreement obtained for the cube diagonal R_{Zr2}, has to be considered with care because of the large incertitude associated with the distance obtained from EXAFS. Basically, the two refinements disagree significantly in the Zr−C distance only. A disagreement close to 0.1 Å for a Zr−C distance around 3 Å is usually not acceptable. This is, however, a peculiar case because a Zr−C distance around 3 Å contributes in the phase uncorrected FT in the 2−3 Å region, i.e., where the experimental signal of the as-prepared UiO-66 MOF is close to the noise level (Figure 6). This is due to the fact that in the same *R*-region, together with the SS (Zr−C−Zr [I_{r} = 31]) path, two 3-bodies MS paths (Zr−C−O−Zr [I_{r} = 36], Zr−O−Oμ_3−Zr [I_{r} = 8]), and a 4-bodies MS path (Zr−C−O−C-Zr [I_{r} = 13]) contribute to the overall

Table 3. Comparison of the UiO-66 Structures as Refined from EXAFS and XRPD Approaches [a]

	hydroxylated							dehydroxylated					
	EXAFS			XRPD *Fm*-3*m* (225)				EXAFS			XRPD *Fm*-3*m* (225)		
neighbor	*D*	R (Å)	<R> (Å)	*D*	R (Å)	<R> (Å)	neighbor	*D*	R (Å)	<R> (Å)	*D*	R (Å)	<R> (Å)
μ_3−O	2	2.087	2.198	4	2.118	2.192	μ_3−O	3	2.06	2.175	4[b]	2.107	2.17
O1	6	2.235		4	2.266		O1	4	2.221		4	2.233	
C1	4	3.19	**3.19**	4	3.105	**3.105**	C1	4	3.17	**3.17**	4	3.255	**3.255**
Zr1	4	3.511	**3.511**	4	3.531	**3.531**	Zr1a	8/3	3.35	3.48	4	3.510	**3.510**
							Zr1b	4/3	3.74				
Zr2	1	4.99	**4.99**	1	4.994	**4.994**	Zr2a	1/3	4.14	4.91	1	4.964	**4.964**
							Zr2b	2/3	5.30				

[a] Listed in order of increasing crystallographic distances from the Zr0 atom are the type of neighbor (see Figure 5 for labels), the degeneration (*D*), and the single (*R*) and averaged (<*R*>) distances. The different symmetries adopted in the two approaches (see text) implies that some bond degenerations may be different. In these cases, the comparison between XRPD and EXAFS should be made on the average distances only. Conversely, when bond degeneration coincides, averaged values are not necessary and are reported in bold. [b] Degeneration of 4, with occupancy factor fixed to 0.75, resulting in an average stoichiometry of 3 μ_3−O ligand per Zr atom.

Table 4. Comparison of the UiO-66 Structures as Refined from B3LYP and XRPD Approaches [a]

	hydroxylated						dehydroxylated				
	periodic B3LYP *F*-43*m* (216)			XRPD *Fm*-3*m* (225)			periodic B3LYP *R*-3 (148)			XRPD*Fm*-3*m* (225)	
neighbor	*D*	R (Å)	<R> (Å)	*D*	R (Å)	neighbor	*D*	R (Å)	<R> (Å)	*D*	R (Å)
μ_3−O	2	2.089				μ_3−Oa	1	2.052			
			2.188	4	2.118	μ_3−Ob	1	2.060	2.116	4[b]	2.107
μ_3−OH	2	2.286				μ_3−Oc	1	2.237			
O1	4	2.249	**2.249**	4	2.266	O1a	1	2.193			
						O1b	1	2.225	2.221	4	2.233
						O1c	1	2.227			
						O1d	1	2.240			
C1	4	3.267	**3.267**	4	3.105	C1a	1	3.203			
						C1b	1	3.214	3.241	4	3.255
						C1c	1	3.243			
						C1d	1	3.305			
Zr1	4	3.571	**3.571**	4	3.531	Zr1a	2	3.462	3.599	4	3.510
						Zr1b	2	3.736			
Zr2	1	5.050	**5.050**	1	4.994	Zr2	1	5.093	**5.093**	1	4.964

[a] Listed in order of increasing crystallographic distances from the Zr0 atom are the type of neighbor (see Figure 5 for labels), the degeneration (*D*), and the single (*R*) and averaged (<*R*>) distances. The use of different space groups in the two approaches (see text) implies that some bond degenerations may be different. In these cases, XRPD distances should be compared with the average values from ab initio calculations. Conversely, when bond degeneration coincides, averaged values are not necessary and are reported in bold. For the hydroxylated material, the optimized cell volume is 8940.8(6) and 9286.6 Å^3 with XRPD and ab initio methods, respectively. For the dehydroxylated material, the optimized cell volume is 8887.3(3) and 9090.8 Å^3 with XRPD and ab initio methods, respectively. [b] Degeneration of 4, with occupancy factor fixed to 0.75, resulting in a stoichiometry of 3 μ_3−O ligand per Zr atom.

signal with comparable intensities (I_r) but significantly different phases. The destructive interference of these four paths results in an almost negligible experimental signal in the 2−3 Å *R*-region that makes signal optimization very critical.[96]

4.2.4. As-Prepared Material: ab initio Optimization of the XRPD Model and Comparison with Experimental Structural Results. The 3-D structure, obtained from the Rietveld refinement in the *Fm*-3*m* space group, was modified in order to model the hydroxylated structure by including the H atoms of the OH groups that could not be localized by XRPD. The first step was to symmetrically include all the eight H atoms (one for each side of the octahedron) in order to preserve the *Fm*-3*m* symmetry of the system. An attempt to optimize such high symmetry system failed because the too high electron density injected by eight OH groups into the inorganic cluster prevents convergence. Removal of four H atoms, in an alternate configuration to minimize the repulsion of the remaining four OH groups (vide supra) implies a symmetry reduction to *F*-43*m* space group (where all clusters maintain the same ordered orientation). A full relaxation (i.e., both cell parameters and atomic positions) was performed by means of periodic ab initio calculations at B3LYP level of theory. At the equilibrium, the cell parameters of the crystallographic cell increased from the starting experimental value of 20.7751(2) to 21.0171 Å: $\Delta a/a = +0.012$.

Table 5. Comparison of the UiO-66 Structures as Refined from B3LYP and EXAFS Approaches. [a]

	hydroxylated						dehydroxylated					
neighbor	periodic B3LYP $F\bar{4}3m$ (216)			EXAFS		neighbor	periodic B3LYP $R\bar{3}$ (148)			EXAFS		
	D	*R* (Å)	<*R*> (Å)	*D*	*R* (Å)		*D*	*R* (Å)	<*R*> (Å)	*D*	*R* (Å)	<*R*> (Å)
μ3−O	2	2.089	**2.089**	2	2.087	μ3−Oa	1	2.052	2.056	2	2.06	**2.06**
						μ3−Ob	1	2.060				
O1	4	2.249	2.268	6	2.235	O1a	1	2.193				
μ3-OH	2	2.286				O1b	1	2.225				
						O1c	1	2.227	2.224	5	2.221	**2.221**
						μ3−Oc	1	2.237				
						O1d	1	2.240				
C1	4	3.267	**3.267**	4	3.19	C1a	1	3.203				
						C1b	1	3.214	3.241	4	3.17	**3.17**
						C1c	1	3.243				
						C1d	1	3.305				
Zr1	4	3.571	**3.571**	4	3.511	Zr1a	2	3.462		8/3	3.35	
						Zr1b	2	3.736	3.599	4/3	3.74	3.48
Zr2	1	5.050	**5.050**	1	4.99	Zr2a	1	5.093	**5.093**	1/3	4.14	4.91
						Zr2b				2/3	5.30	

[a] Listed in order of increasing distances from the Zr0 atom (acting as absorber for EXAFS) are the type of neighbor (see Figure 5 for labels), the degeneration (*D*), and the single (*R*) and averaged (<*R*>) distances. Because of the inability of EXAFS to discriminate too close bond distances, some sets of ab initio distances were averaged. When the averaging process has not been adopted, corresponding <*R*> values are reported in bold. For error bars associated to the EXAFS refinement, please refer to Table 2. EXAFS refinement was obtained using as input model the optimized structure from XRPD and from ab initio calculations for the hydroxylated and dehydroxylated forms, respectively.

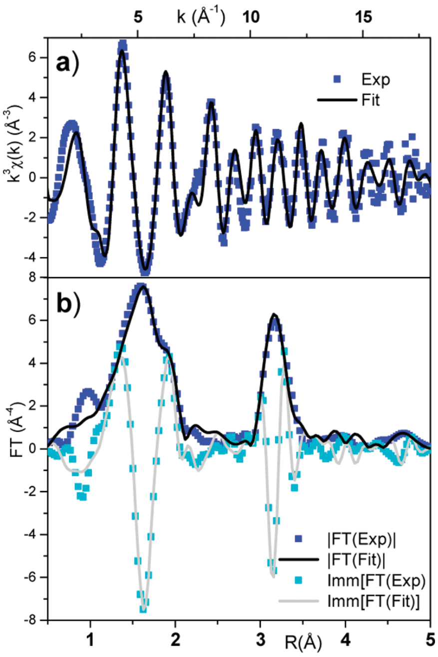

Figure 6. (a): Comparison between experimental (scattered squares) and best fit (full line) k^3-weighted $\chi(k)$ of the as-prepared (hydroxylated) UiO-66 material. (b): As panel (a) in *R*-space (both moduli and imaginary parts are reported). The 3-D structure obtained from the XRPD Rietveld refinement in the $Fm\bar{3}m$ space group was used as the input model for the EXAFS refinement.

Summarizing, ab initio optimization of the hydroxylated structure was made in a space group (*F*-43*m*) of higher symmetry with respect to the actual structure (showing random orientation of the inorganic clusters) but of lower symmetry with respect to that we were forced to use in the XRPD refinement. Consequently, care must be taken when comparing structural parameters such as atomic distances obtained with the two approaches. The same holds true when a comparison is made with EXAFS results that are sensitive to the local order of the individual cluster only, irrespective of their orientation in the crystallographic cell. Considering only the first shell Zr−O distances, XRPD discriminates between four equivalent μ_3−O atoms and four equivalent O1 atoms of the carboxylate units, while ab initio calculations, performed with a lower symmetry, are able to discriminate between two μ_3−O atoms and two μ_3−OH atoms. EXAFS does not care about long-range symmetry and differentiates Zr−O contributions that are sufficiently different in terms of bond distance, resulting in two short contributions due to μ_3−O atoms and six long contributions due to the merging of two μ_3−OH and four O1 atoms.

As mentioned, the B3LYP optimized distances between Zr0 and μ_3−O, μ_3−OH, and O1 atoms have to be averaged differently when a comparison is made between XRPD and EXAFS values because the two experimental techniques discriminate differently among the three components. The same holds for higher shells distances. For this reason, two tables are presented to compare experimental and theoretical results. Computed distances are compared with XRPD and EXAFS in Tables 4 and 5, respectively. From now on, all distances between the Zr0 atom (absorbing atom for EXAFS) and the generic neighbor atom A (labeled in Figure 5a,b and used in Tables 4 and 5) will be referred as R_A.

While EXAFS and ab initio results agree in predicting the shortest μ_3−O distance (2.087 vs 2.089 Å), XRPD overestimates it (2.118 Å). This is due to the fact that XRPD averages between $R_{\mu3-O}$ and

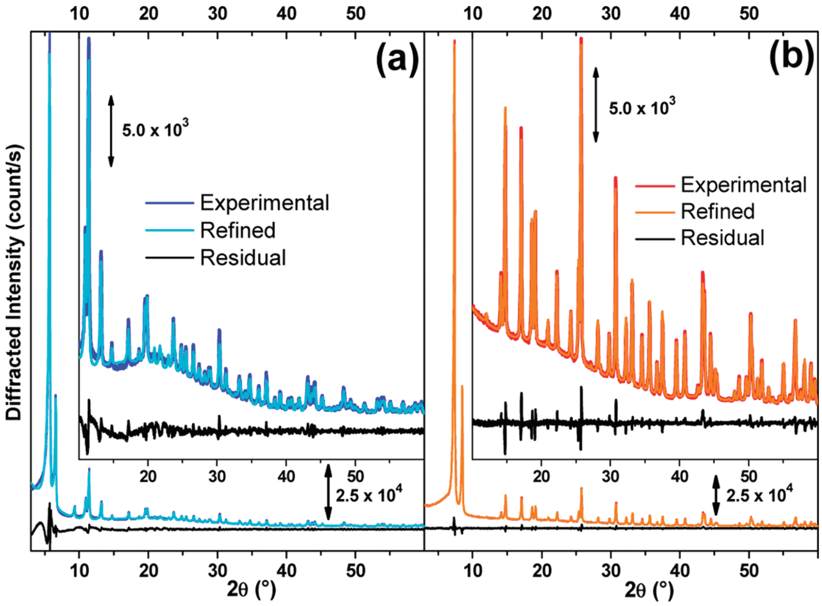

Figure 7. (a): Rietveld refinement of hydroxylated UiO-66 material. Experimental, calculated, and residual patterns are reported as blue, cyan, and black curves, respectively. (b): Final Rietveld plot of dehydroxylated UiO-66 material (sample was treated at 300 °C and sealed inside a capillary to prevent readsorption of water). Experimental, calculated, and residual patterns are reported as red, orange, and black curves, respectively. In both cases, the refinement has been performed in the *Fm*-3*m* space group (λ = 1.5406 Å); the zooms report the magnification of the high-angle scattering profile.

$R_{\mu 3-\mathrm{OH}}$ that are longer (2.286 Å from ab initio calculations). In fact, when a comparison is made with the R_{O1}, that is not affected by degeneration problems, the agreement is much better: 2.249 vs 2.266 Å for ab initio and XRPD approaches, respectively. EXAFS merges μ_3−OH with O1 distances at 2.235 Å. The worst agreement is found for R_{C1}: 3.267, 3.105, and 3.19 Å for ab initio, XRPD, and EXAFS, respectively. In particular, both experimental values are underestimated with respect to the B3LYP predicted R_{C1} value obtained modeling a perfect lattice. This systematic disagreement can be partially understood by considering that about one BDC linker out of 12 is missing (see Figure 3 and related discussion). Obviously, the lack of a BDC unit will affect, among all distances of the $Zr_6O_4(OH)_4$ octahedron, mainly the distances between the Zr atom at the missing site and the two O1 atoms of the remaining BDC unit that are expected to contract. Coming to the octahedron side (R_{Zr1}) and diagonal (R_{Zr2}), both computed values are overestimated by about 0.05 Å with respect to the experimental ones that are in relative nice agreement. Being that $\Delta R/R$ is within 1.5%, the disagreement between theory and experiment is within the accuracy of B3LYP level of theory.[97,98] Note also that, for symmetry reasons imposed by the adopted *Fm*-3*m* and *F*-43*m* space groups, both XRPD and ab initio approaches optimized the $Zr_6O_4(OH)_4$ octahedron with the constrain $R_{\mathrm{Zr2}} = (2R_{\mathrm{Zr1}})^{1/2}$. EXAFS refinement, that refines these two distances independently, confirms that this model holds: R_{Zr2} = 4.99 ± 0.04 Å, while $(2R_{\mathrm{Zr1}})^{1/2}$ = 4.97 ± 0.01 Å.

4.3. Dehydroxylated Material: XRPD, EXAFS, IR, and ab initio Combined Structure Refinement. As already anticipated in Section 4.2.2, the UiO-66 structure was solved first from the XRPD pattern of its dehydroxylated form. The absence of electronic density inside the pores implies that all electron density corresponds to ordered framework atoms and will thus be easier refined. Extractions of the peak positions, pattern indexing, and Rietveld refinements were carried out with the TOPAS program.[62,63] A face-centered cubic unit was found unambiguously with satisfactory figure of merit (M_{20} = 63). No extra systematic extinctions were observed, and the most symmetric *Fm*-3*m* space group was first chosen to solve the structure. Calculations were performed with the EXPO package, using EXTRA for extracting integrated intensities and SIR97 for direct methods structure solution.

The structure solution in space group $Fm\bar{3}m$ (No. 225) gave directly all atoms in the asymmetric unit. This model was used as a starting point for the Rietveld refinement. At the final stage, Rietveld refinement involved the following parameters: 8 atomic coordinates, 4 thermal factors, 1 scale factor, 1 zero point, 1 cell parameter, 29 background parameters, and 7 ones to model the evolution of asymmetric diffraction lines shape. The final Rietveld plot (Figure 7b) corresponds to satisfactory crystal structure model indicator (R_{Bragg} = 0.011) and profile factors (R_{P} = 0.016 and R_{WP} = 0.022).

TGA data show that two H_2O per $Zr_6O_4(OH)_4$ cluster leave the structure when the material is heated above 250 °C (Figure 2b,c), and at 300 °C, no residual OH groups can be observed with IR (see inset of Figure 4b). EXAFS confirms the loss of about one oxygen in the first coordination sphere of Zr atoms, moving from 8- to 7-fold coordination. Panel (a) of Figure 8 reports a schematic representation of the dehydroxylation process of UiO-66, where each inorganic $Zr_6O_4(OH)_4$ cluster rearranges into a distorted Zr_6O_6 cluster.

The dehydroxylated Zr_6O_6 cluster has a *D*3*d*(−3 m) symmetry, showing a preferential squeezing direction, corresponding to one out of the three octahedron diagonals (Figure 8b,c). On the local ground seen by EXAFS, the same experimental spectrum is obtained independently on which, out of the three diagonals, is the squeezing direction. Conversely, the relative orientation of the adjacent squeezed clusters affects the XRPD datum. If all four clusters in the unit cell are oriented in the same direction, the dehydration changes the symmetry of the structure to *R*-3*m* (No. 166). This structure was optimized with force field based molecular modeling (Forceit, Accelrys MS 4.3). A small deviation from trigonal symmetry is then expected, but no

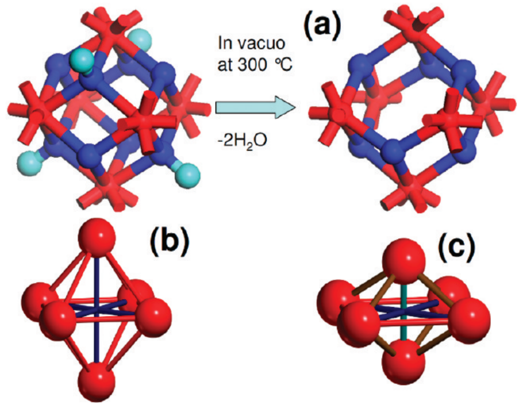

Figure 8. (a): Stick and ball representation of the dehydroxylation undergone by the inorganic $Zr_6O_4(OH)_4$ cluster upon thermal treatment at 300 °C in vacuo resulting in a distorted Zr_6O_6 cluster. Red, blue, and cyan colors refer to Zr, O, and H atoms, respectively. (b): Stick and ball representation of the perfect Zr_6 octahedron, showing 12 equivalent R_{Zr1} sides and thee equivalent $R_{Zr2} = (2\,R_{Zr1})^{1/2}$ diagonals. (c): Stick and ball representation of a squeezed Zr_6 octahedron. The 12 sides are now split into four in-plane long R_{Zr1b} sides and eight prismatic short R_{Zr1a} sides, while the three diagonals evolve into two in-plane long R_{Zr2b} and one orthogonal short R_{Zr2a} diagonals. For clarity, O and H atoms are omitted in panels (b) and (c).

deviation from the cubic symmetry was observed. This again makes it more probable that the clusters are randomly oriented in the structure.

The dramatic modification undergone by the EXAFS spectrum upon dehydroxylation (Figure 4c and Table 2) is basically explained in terms of three main effects: (i) small contraction of the first Zr—O shell accompanied by a small decrease in coordination (erosion of the shoulder around 1.9 Å); (ii) relevant distortion of the second shell contribution showing a maximum that moves from 3.17 to 2.91 Å, with a shoulder at 3.41 Å, thus reflecting an important splitting of the R_{Zr1} distances of the octahedron sides; and (iii) the almost complete disappearance of the weak contribution around 4.7 Å due to the Zr—Zr SS signal of the octahedron diagonal (R_{Zr2}). As extensively described in Sections 4.2.1—4.2.4, a more accurate optimization of the EXAFS data requires the knowledge of a 3-D cluster simulating the local environment around Zr0 atom. Differently to the hydroxylated case, the 3-D model obtained from the Rietveld refinement of XRPD data in the highly symmetric $Fm\bar{3}m$ space group was inadequate to simulate the experimental datum. The origin of this failure was obviously due to the inability of the model to account for two different R_{Zr1} (and possibly R_{Zr2}) distances. The failure of the XRPD model was overcome by using the optimized geometry obtained by ab initio periodic calculations, as outlined in the following.

The dehydroxylated structure was then modeled at B3LYP level of theory. From the description of the change in zirconium coordination from 8 to 7, as revealed from experimental results upon dehydration (Figure 2d in ref 39), the new structure was designed removing from the $Zr_6O_4(OH)_4$ cluster two water molecules, according to the scheme reported in panal (a) of Figure 8. The structure was successfully fully relaxed (resulting in optimized atomic positions and cell parameter), and the new symmetry sorted out (*R*-3*m*, No. 166). When frequency calculation was performed to study vibrational modes (Section 5.1), one negative frequency showed up, indicating that the optimized geometry in the *R*-3*m* space group did not correspond to a global minimum but to a transition state. A deeper investigation was accomplished by exploring the energy and the geometry of the system along the selected negative normal mode to sort out the correct symmetry group. This step is done automatically by the CRYSTAL code. At that stage, the new geometry was reoptimized in the new subgroup and vibrational frequencies reevaluated. It was found that the new structure, which belongs to the trigonal *R*-3 (No. 148) space group, was a minimum, thus showing only positive frequencies. The final system shows 18 irreducible atoms in the primitive cell (still 6 symmetry operators are present) and a difference in volume less than 0.5% with respect to the *R*-3*m* structure. Structural analysis shows that the symmetry breaking lays in a predominant off-plane deformation of the phenyl group that only marginally modifies the structure of the metal cluster. IR and Raman (not reported here for brevity) spectra were calculated and will be discussed in Section 5.1.

As already anticipated the 3-D structure obtained from the XRPD refinement, in the *Fm*-3*m* space group was unable to reproduce the high-*R* tail of the Zr—Zr signal in the 3.3—4.0 Å region because only one R_{Zr1} contribution ($N = 4$) was foreseen in the model. Only the 2.6—3.3 Å region was correctly reproduced. Moreover, the refined distance ($R_{Zr1} = 3.33 \pm 0.02$ Å) was 0.20 Å shorter than that found by XRPD, and the corresponding Debye—Waller factor, $\sigma^2(Zr1) = 0.014 \pm 0.002$ Å^2, was twice that found for the hydroxylated form. Using the 3-D structure as fully optimized by ab initio calculations in the trigonal *R*-3 space, the whole 2.6—4.0 Å region was correctly reproduced with two shells characterized by $R_{Zr1a} = 3.32 \pm -0.01$ Å, $\sigma^2(Zr1a) = 0.008 \pm 0.001$ Å^2 with $N = 2$ and $R_{Zr1b} = 3.73 \pm 0.02$ Å, $\sigma^2(Zr1b) = 0.012 \pm 0.003$ Å^2 with $N = 2$. The improvement of the fit was significant, but the value of the Debye—Waller of the longer octahedron side was still too high. Additional problems came when the contribution of the octahedron diagonal (R_{Zr2}) was optimized. The fit showed clear instabilities, and the optimized R_{Zr2} distance was either significantly shorter or significantly longer than the value optimized at B3LYP level depending on the starting value. This evidence suggests that the Zr_6O_6 deformed octahedron exhibits two significantly different diagonals, as was the case of the sides.

The perfect Zr_6 octahedron (Figure 8b), shows 12 equivalent R_{Zr1} sides and three equivalent $R_{Zr2} = 2^{1/2}\,R_{Zr1}$ diagonals. The simplest model to account for a distortion of the Zr_6 octahedron is to assume that the four in-plane Zr still form a square, while the two apical ones are either squeezed or stretched in the perpendicular axis. In the former case (Figure 8c), deformation results in the splitting of the 12 sides into four in-plane long R_{Zr1b} sides and eight prismatic short R_{Zr1a} sides, while in the latter case an opposite situation occurs, with long R_{Zr1b} sides (the prismatic ones) twice more abundant than short R_{Zr1a} sides (the in-plane ones). As the experimental EXAFS datum clearly indicates that the R_{Zr1a} signal is much more intense than the R_{Zr1b} one, the former model is adopted that also implies an evolution of the three diagonals into two in-plane long R_{Zr2b} and one orthogonal short R_{Zr2a} diagonals. According to this model, geometrical constrains among sides and diagonals are $R_{Zr2b} = (2\,R_{Zr1b})^{1/2}$ and $R_{Zr2a} = [4\,R^2_{Zr1b} - R^2_{Zr2b}]^{1/2}$. The final optimization of the EXAFS signal was so performed starting from the ab initio optimized *R*-3 structure with the following two modifications: (i) the degeneration of Zr1a and Zr1b SS paths was changed from $N_{Zr1a} = N_{Zr1b} = 2$ to $N_{Zr1a} = 8/3$ and $N_{Zr1b} = 4/3$, and (ii) the single degenerated Zr2 path was split into a short ($N_{Zr2a} = 1/3$) and a long one ($N_{Zr2b} = 2/3$). To limit the

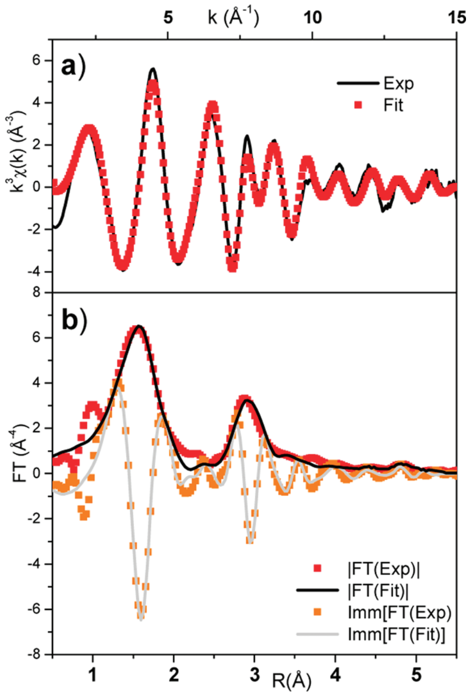

Figure 9. (a): Comparison between experimental (scattered squares) and best fit (full line) k^3-weighted $\chi(k)$ of the dehydroxylated UiO-66 material. (b): As panel (a) in R-space (both moduli and imaginary parts are reported). The 3-D structure obtained from the ab initio optimization, performed at B3LYP level, in the $R\bar{3}$ space group was used as input model for the EXAFS refinement, with the only exceptions of the two R_{Zr} contributions. The fitting of the shorter R_{Zr1a} and R_{Zr1b} distances is done fixing the EXAFS coordination numbers to 8/3 and 4/3, respectively (being 2 the degeneration in the ab initio calculations). The fitting of the longer R_{Zr2} distance (three diagonals of the Zr_6 octahedron) could be possible only splitting the contribution into a short axial diagonal and (R_{Zr2a}, involving two Zr atoms out of six; $N = 1/3$) and two long diagonals (R_{Zr2b}, involving four Zr atoms out of six; $N = 2/3$).

number of optimized parameters S_0^2 and ΔE_0 were fixed to the values optimized for the hydroxylated material (no edge shift was observed by XANES (Figure 4b). The quality of the fit can be appreciated in Figure 9 and which results were reported in Tables 2 and 5.

On the basis of the XRPD, ab initio, and EXAFS refined geometries, as summarized in the right parts of Tables 3, 4 and 5, a comparative discussion of the structural results obtained with the three approaches can be faced. According to what was discussed for the hydroxylated case (Section 4.2.4), ab initio distances were averaged differently in order to be directly comparable with XRPD or EXAFS results. For symmetry reasons, XRPD refined three equivalent $\mu_3{-}O$ distances at 2.107 Å, in fair agreement with ab initio results (2.116 Å). Such a value comes from averaging two short ($\mu_3{-}Oa$ and $\mu_3{-}Ob$) and a long distance ($\mu_3{-}Oc$), the latter being sufficiently stretched (2.237 Å) to fall in the region of the Zr−O1 distances. For this reason, EXAFS refinement gives a much shorter $R_{\mu3-O}$ value (2.06 Å) that is, however, in perfect agreement with the average of the $R_{\mu3-Oa}$ and $R_{\mu3-Ob}$ values refined in the ab initio calculations (2.056 Å). Coming from the distances with the four oxygen atoms of the carboxylate units, XRPD, ab initio, and EXAFS results in R_{O1} values of 2.233, 2.221, and 2.221 Å, respectively, the latter value also including the longer $\mu_3{-}Oc$ distance. An excellent agreement is obtained by XRPD and ab initio in determining the distance with the C atoms of the carboxylate units: 3.255 and 3.241 Å, respectively. EXAFS refinement is unable to reproduce correctly the R_{C1} value (3.17 Å) because of a destructive interference with some MS paths as outlined at the end of the Section 4.2.3. The high symmetry of the XRPD model imposes a single octahedron side R_{Zr1} = 3.510 Å that agrees well with the averaged value coming from EXAFS approach: 3.48 Å. Ab initio and EXAFS approaches, that are able to observe the splitting of the octahedron edges (but with different degeneration), agree on the long value (R_{Zr1b} = 3.736 and 3.74 Å, respectively), while disagree significantly on shorter one (R_{Zr1a} = 3.462 and 3.35 Å, respectively). Finally, the octahedron diagonal is estimated to be R_{Zr2} = 4.964 and 5.093 Å for the XRPD and ab initio approaches, respectively. EXAFS is the only technique that, having no symmetry constrain, is able to observe the octahedron diagonal splitting. Optimized values are $R_{Zr2a} = 4.14 \pm 0.07$ Å ($N_{Zr2a} = 1/3$) and $R_{Zr2b} = 5.30 \pm 0.04$ Å ($N_{Zr2b} = 2/3$), respectively. The average value $<R_{Zr2}>$ = 4.91 Å is in fair agreement with the XRPD distance (4.964 Å), while is significantly underestimated with respect to the ab initio value (5.093 Å). Comparison with the geometrical consideration is very good: expected $R_{Zr2b} = (2\ R_{Zr1b})^{1/2}$ = 5.29 and $R_{Zr2a} = [4\ R^2_{Zr1b} - R^2_{Zr2b}]^{1/2}$ = 4.11 Å, meaning that the model of the axially squeezed Zr_6 octahedron (Figure 8c) is fully compatible with the EXAFS data. It must however be considered that this model is highly supported by the EXAFS analysis of the side lengths (as the EXAFS signal associated with R_{Zr1a} and R_{Zr1b} SS paths is strong), while the additional agreement obtained by analyzing the much weaker diagonal signal, although elegant, adds only little significance to the model.

Any attempt to refine the XRPD data in a space group with lower symmetry ended up with a structure similar to that refined in the *Fm*-3*m* space group and with an higher correlation among optimized parameters, without any additional information. This indicates that the squeezing direction occurs randomly in the solid (yellow arrows in Figure 1c).

5. VIBRATIONAL AND ELECTRONIC PROPERTIES: EXPERIMENTAL VERSUS AB INITIO RESULTS

5.1. IR Characterization of the Lattice Vibration: Effect of Solvent Removal and Rehydration.

IR spectroscopy can be of great help in the characterization of MOF materials.[99] The IR spectra reported in Figure 10 summarizes the effect on the vibrational properties of solvent removal and progressive dehydration (top part) and successive rehydration (bottom part) of UiO-66. Panels (a) and (b) refer to the OH and framework stretching modes, respectively. For sake of simplicity, we will discuss panel (a) and panel (b) separately, even if the data were collected simultaneously in the two spectral ranges.

Bold black curve in panel (a) of Figure 10 illustrates the IR spectrum of a thin film of the UiO-66 sample, prepared by deposition on a silicon wafer of Zr−MOF sample placed in water suspension. The spectrum is dominated by an intense and broad band centered at 3450 cm^{-1} due to intercrystallite water (used for preparing the deposition) and physisorbed water condensed inside the crystal cavities. A minor but much sharper component at 3675 cm^{-1} corresponds to a small fraction of isolated OH groups (mainly present on the external surfaces of the microcrystals), while in the 3100−2850 cm^{-1} interval weak bands due

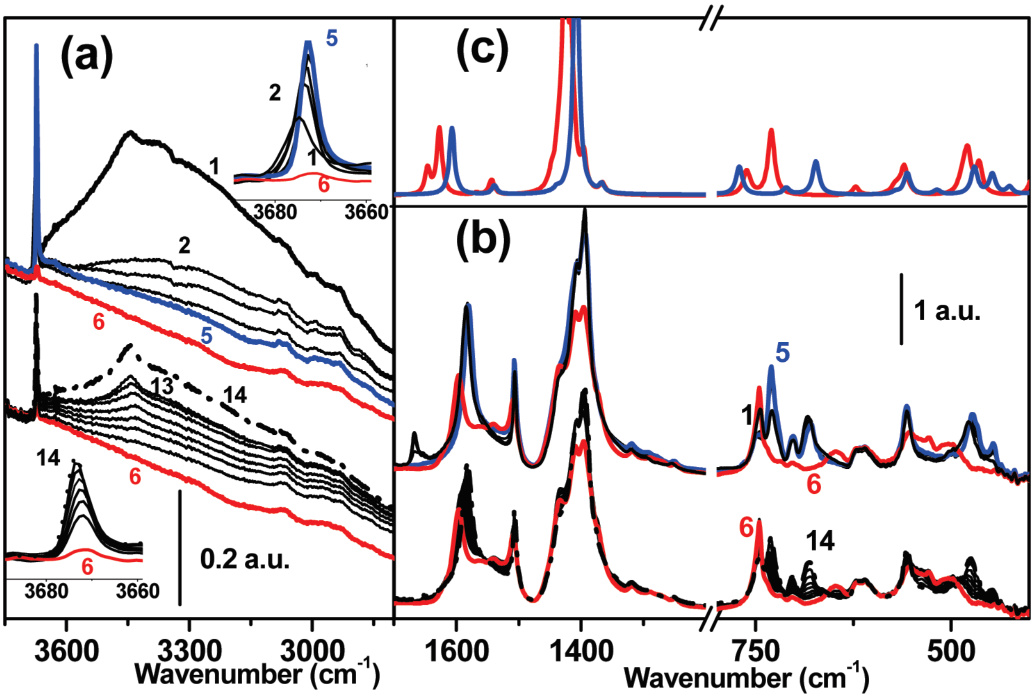

Figure 10. (a): Effect of dehydration (top parts) and rehydration (bottom parts) on the IR curves in the O−H stretching region; curve 1 (as-prepared sample), curve 2 outgassed at room temperature 1′, curve 3 outgassed at room temperature 10′, curve 4 outgassed at 150 °C for 30 min, curve 5 outgassed at 250 °C for 30 min, curve 6 outgassed at 300 °C for 30 min, and curves 7−14 effect of progressive rehydration (curve 14 was collected after 8 h). (b): As panel (a) in the skeletal modes region. (c): Computed IR spectra of hydrated (blue) and dehydrated (red) forms, optimized in the *F*-43*m* and *R*-3 space groups, respectively. Experimental (panel b) and computed (panel c) spectra were reported on the same wavenumber range and scale to allow direct comparison. No scaling factor has been adopted.

to aromatic and aliphatic ν(C−H) modes of benzene ring and DMF are visible. The effect of progressive outgassing at room temperature (1 and 10 min), 150 °C and at 250 °C is illustrated by red curves 2−5, respectively. The relevant decrease of the band centered at 3450 cm^{-1}, upon an outgassing of 1 min at room temperatrure (curve 2) is mainly due to removal of intercrystallite water; parallel growth of the component due to isolated OH groups (sharp peak at 3672 cm^{-1}) present on the external surfaces is also observed. Successive outgassing for increased time (curve 3) and heating (curves 4−5 until 250 °C) erodes nearly completely the band at 3450 cm^{-1} and causes the growth of the peak at 3672 cm^{-1}. A thermal treatment in high vacuo for 30 min at 300 °C gives rise to the red curve reported in panel (a) of Figure 10. In this case, very few OH groups are left, and only weak bands due to the CH modes are present. Rehydration effects on the IR spectra of Zr−MOF are illustrated in the bottom part of panel (a) of Figure 10, curves 6−14. The last spectrum was obtained after 8 h (black curve dashed dotted). Under these conditions, UiO-66 is progressively rehydrated (growth of the peak at 3672 cm^{-1} and of band centered at 3450 cm^{-1}). The uncompleted restoration of spectrum 1 (full line black curve) is due by the fact that it was obtained on a sample soaked in water, while only vapor tension is dosed on the rehydration step.

The high stability of the framework with respect to water solvent (already tested by XRPD, see Figure S2a of the Supporting Information) is confirmed by IR data that show complete reversibility of the dehydration/hydration phenomenon. The IR spectra reported at the bottom part of panel (b) of Figure 10 testify that the spectrum obtained upon rehydration is completely equivalent to that collected on the starting sample (compare black curves full line and dashed dotted lines).

Table 6. Selection of Calculated Harmonic Vibrational Modes (cm^{-1}) Compared for the Two Structures. [a]

hydroxylated	dehydroxylated	description
1607	1568−1627−1648	OCO asymmetric stretching (in-phase/antiphase)
1539	1541−1545	CC ring
1408	1412−1426	OCO symmetric stretching
1367	1364−1367	CC ring
814	−	OH bending + CH bending (antiphase)
771	762	OH bending + CH bending (in-phase)
711	−	OH bending + CC ring + OCO bending
673	730	μ_3−O stretching
−	622	Zr−(OC) symmetric stretching
556	560	Zr−(OC) asymmetric stretching
518	−	out-of-plane ring deformation
470	−	μ_3−OH stretching (in-phase)
−	490−464	out-of-plane ring deformation
447	−	μ_3−OH stretching (antiphase)
425	−	μ_3−OH stretching

[a] See panel (c) of Figure 10 for a graphical representation of the calculated spectra. No scaling factor has been adopted. Refer to the CRYSTAL Web site[101] for the full calculated spectra (IR and Raman, the latest not discussed here for brevity).

The black curve in panel (b) of Figure 10 reports the IR spectrum in the skeletal modes region of the as-prepared sample.

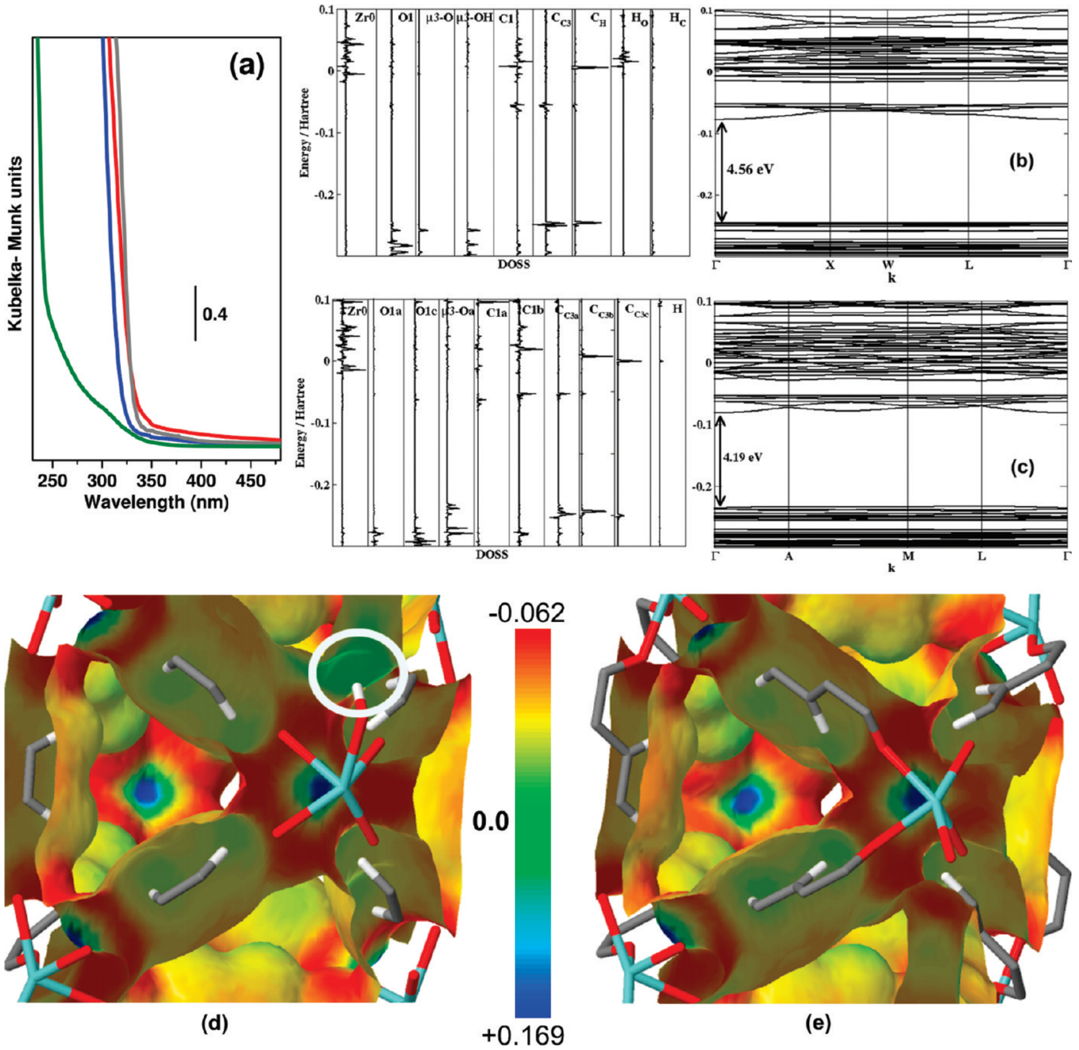

Figure 11. (a): DRS UV−vis spectra of UiO-66 as synthesized (blue curve), dehydroxylated UiO-66 (red curve), disodium terephthalte-DSTA (gray curve), and monoclinic ZrO_2 (green curve). (b) left: Computed electron density of states of hydroxylated UiO-66 projected on the different atoms labeled as in Figure 5. Total energy in Hartree. (b) right: Corresponding band structure. Band gaps in eV. (c): Panel (b) for the dehydroxylated form. (d): Details of the 3-D electrostatic potential mapped on the charge density iso-surfaces for UiO-66 MOF in its hydroxylated form. (e): Panel (d) for the dehydroxylated form. Red, green, and blue zones represent negative, zero, and positive potential values, reported in atomic units, respectively. Comparison between panels (d) and (e) allows appreciation of the differences arising upon removal of the OH group (evidenced by the white circle).

Table 7. Band Gaps (eV) for the Two Forms of UiO-66 and Three Phases of ZrO_2

system	experimental	calculated
UiO-66 hydroxylated	4.07[a]	4.56[a]
UiO-66 dehydroxylated	3.94[a]	4.19[a]
ZrO_2 cubic	–	6.54[a], 5.55[b]
ZrO_2 monoclinic	5.19[a], 5.20[c]	6.32[a], 5.42[b]
ZrO_2 tetragonal	–	6.79[a], 6.40[b]

[a] This work. [b] Plane wave pseudopotential fixing the lattice parameters at the experimental values.[102] [c] Vacuum UV spectroscopy.[103]

The band at 1667 cm^{-1} is ascribed to DMF, while the intense doublet at 1589 and 1395 cm^{-1} is associated to the in- and out-of-phase stretching modes of the carboxylate group. At lower frequencies, modes due to OH and CH bending are mixed with Zr−O modes (main bands at 746, 726, 702, 683, 614, 556, and 475 cm^{-1}). In ZrO_2, a triplet at 725, 620, and 530 cm^{-1} was assigned to longitudinal and transverse modes, respectively.[100] Upon a progressive outgassing (spectra 2−6) the main changes observed can be summarized as follows: (i) disappearance of the band at 1667 cm^{-1} due to DMF, (ii) perturbation of the carboxylates modes, in particular the asymmetric component decreases in intensity and blue shifts, and (iii) substantial changes in the 800−400 cm^{-1} interval, where the peak at 746 cm^{-1} grows, the bands at 726, 702, 683 cm^{-1} disappear, the component at 556 cm^{-1} decreases in intensity and a new component appears at 526 cm^{-1}, while the band at 475 cm^{-1} shifts to 502 cm^{-1} becoming less intense and broader. The substantial changes in the skeletal modes of UiO-66 that occur upon activation at 300 °C can be justified by considering the relevant distortion of the $Zr_6O_4(OH)_4$ cluster that rearranges into a distorted Zr_6O_6 cluster (Figure 8). In previous studies on other MOF materials, modifications of the framework vibrational features upon solvent removal have already been observed and justified by the rearrangement of the structure upon water removal.[88,92,94] In this case, however, the changes are more relevant as the extraction of two out of the eight μ_3−O of the inorganic clusters occurs. Structural data have shown that the removal of bridging μ_3−OH groups causes a relevant loss in the local symmetry of the units (Section 4.3). This has an effect on the vibrational properties as illustrated in panel (c) of Figure 10 that compares the computed IR spectra at the B3LYP level of theory in the case of hydroxylated and dehydroxylated sample (blue and red curves, respectively). In particular, note the fate of the band at 673 cm^{-1}, associated to μ_3−O stretching, that shifts up to 730 cm^{-1} in the case of the dehydroxylated material and the disappearance of the component at 470 cm^{-1} ascribed to the (HO)−Zr−(OH) bending mode. Experimental and computed spectra are in very good agreement, thus allowing an assignment of the main observed IR peaks. Selected calculated vibrational frequencies and the description of the corresponding normal modes are reported in Table 6. Modes animation can be visualized at the CRYSTAL Web site.[101]

5.2. Material Band Gap UV−Vis and Electrostatic Potential. DRS UV−vis spectra of hydroxylated and dehydroxylated UiO-66 are compared in panel (a) of Figure 11, blue and red curves, respectively. Spectra of disodium terephthalate (gray curve) and of bulk ZrO_2 (green curve) are also reported for sake of comparison (Table 7). UiO-66 spectra are characterized by an absorption edge around 310 nm ascribed to $\pi-\pi^*$ electronic transitions of the aromatic ring. The red shift, with respect to the $\pi-\pi^*$ transitions of benzene, is a consequence of the conjugation with the two carboxylate groups, as testified by the spectrum of the terephtalate (gray curve). Electronic transitions involving the metal cluster are not visible as they occur at much higher energy: ZrO_2 (green curve) spectrum shows an edge at 239 nm, associated to $O^{2-}Zr^{4+} \rightarrow O^{-}Zr^{3+}$ LCMT transition. Sample activation induces a small blue shift of the edge that moves from 305 to 315 nm.

On a computational ground, the energy gap (E_g) was computed first for the three forms of ZrO_2 to verify the validity of the adopted level of theory. In agreement with the results of Kralik et al.,[102] who adopted a plane wave approach, we found that the zirconia E_g increases in the order of monoclinic < cubic < tetragonal (Table 7). Comparison with the experimental E_g value for the monoclinic phase results in an overestimation of about 22%, confirming the general overestimation of E_g computed at B3LYP level.[104−106]

The experimental shift of E_g, undergone by UiO-66 by dehydroxylation, is confirmed by the calculated values that lower from 272 nm (4.56 eV) to 296 nm (4.19 eV) (see right parts of Figure 11b,c and Table 7). From the analysis of the density of states projected on the different atoms of the framework (see left parts of Figure 11b,c), the origin of the band gap tuning upon dehydroxylation is disclosed. In both hydroxylated and dehydroxylated cases, the carbon atoms of the organic linker are those involved in the modulation of the band gaps, while Zr atoms do not play any role. This result is similar to that obtained for MOF-5 structure.[57]

Interestingly, the E_g of UiO-66 and MOF-5 show different behaviors with respect to those of their corresponding oxides (i.e., ZrO_2 and ZnO). For MOF-5, the presence of valence electronic bands in the gap due to the organic linkers leads to an increase of the computed E_g (from 3.4 eV for ZnO to 5.0 eV), while for UiO-66 this causes an E_g reduction (from 6.3 to 4.5 eV). Consequently, the role of the organic linker to define the band gap of the MOF suggests that its functionalization[42−46] and/or interaction with adsorbed molecules are a mean to tune MOF's band gaps, opening a way for optical and sensoring applications.

The electrostatic potential was calculated and mapped on a charge density iso-surface of 0.003 |e|. Three-dimensional maps are reported in panels (d) and (e) of Figure 11 for the hydroxylated and dehydroxylated UiO-66 structures, respectively. Red, green, and blue regions represent negative, zero, and positive values, respectively. In panel (d), a prominent neutral zone (green spot) shows up corresponding to the hydrogen atom in the inorganic brick of the hydroxylated system. Nevertheless, in both pictures, the positive areas around the zirconium atom (blue spots) are very similar, while the negative zone (red spots) in panel (d) looks stronger than in panel (e). Comparison between panels (d) and (e) allows for a qualitative view on the electronic rearrangement undergone by the $Zr_6O_4(OH)_4$ unit upon dehydroxylation. On top of this, such qualitative pictures can be of help in the identification of preferential adsorption sites for small molecules; nevertheless, in the present case, the high packing of the $Zr_6O_4(OH)_4$ and Zr_6O_7 units (that are linked to 12 BDC units) do not allow access to the metal centers. Molecular adsorption is then expected to occur mainly on the BDC linkers.

6. SUMMARY AND CONCLUSIONS

We reported a detailed study of the structural, vibrational, and electronic features of UiO-66 (Zr-BDC MOF) in its hydroxylated and dehydroxylated forms as obtained through the combination of experimental and theoretical approaches such as XRPD, EXAFS, IR, and UV−vis spectroscopies and ab initio periodic DFT calculations. This knowledge is important because the determined thermal stability of this MOF and its resistance to aggressive chemical solvents, makes UiO-66 a potential candidate for practical applications, e. g., in catalysis or photocatalysis.[42−46]

(i) The stability properties of UiO-66 were outlined in details: temperature-dependent XRPD was performed to confirm the crystallinity of the material in air up to 375 °C, and thermo-gravimetric analysis, that showed a progressive structured weigh loss up to 300 °C, was combined with mass spectroscopy experiment to confirm the loss of physisorbed water first and DMF molecules afterward. More than 70% of the starting weight was reported to be still preserved up to 500 °C, where loss of benzene fragments starts and the structure collapses leaving a low crystalline ZrO_2. An accurate determination of the weight loss at this final stage, allowed an estimation of the material defectivity, measuring the drift of the BDC/$Zr_6O_4(OH)_4$ ratio from 12. Stability was checked with respect to water, benzene, acetone, ethanol, a strong acid such as HCl, and a strong base as NaOH.

(ii) The structure of both hydroxylated and dehydroxylated forms was refined through an interactive XRPD/EXAFS approach. The different evolution of the XRPD pattern and EXAFS spectra upon solvent removal was described in detail, showing how the material evolves differently on local and long-range levels. Solvent removal implies the loss of structural μ_3−OH groups from the ordered $Zr_6O_4(OH)_4$ cluster into a distorted Zr_6O_6 cluster, i.e., from T_d (−43 m) to D_{3d} (−3 m) symmetry. Zr atoms changes from 8- to 7-fold coordination. IR spectra confirmed the full removal of OH groups. The final accepted models satisfied both XRPD and EXAFS evidence and were used as input for periodic ab initio calculation to further verify the validity of the structures.

(iii) For both forms of UiO-66, ab initio structural distances were compared with XRPD and EXAFS data separately to take into account that the distances obtained by the two experimental techniques are different in systems where local and long-range order behave differently.[47−53] For this reason, distances obtained at B3LYP level were averaged differently when compared with the experimental XRPD and EXAFS values (Tables 4 Table 5, respectively).

(iv) *Hydroxylated case:* EXAFS and ab initio techniques agreed in the determination of the μ_3−O distance, while XRPD (not able to discriminate between $R_{\mu3-\mathrm{O}}$ and $R_{\mu3-\mathrm{OH}}$) overestimated it; on the other hand, calculated R_{O1} distances agreed with those observed by XRPD, while EXAFS, merging μ_3−OH and O1, overestimated them. Observed R_{Zr1} and R_{Zr2} were very similar, showing a 1.5% disagreement with respect to the calculated result.

(v) *Dehydroxylated case:* For XRPD, three equivalent $R_{\mu3-\mathrm{O}}$ exist that well matched with ab initio results (able to take into complete account the symmetry breaking of the system). In this case, EXAFS saw only two out of three μ_3−O distances that, nevertheless, agreed very nicely with the calculated one; the remaining $R_{\mu3-\mathrm{O}}$ laid in the range of the four oxygen atoms of the carboxylate units, leading to an average value slightly smaller than those obtained with XRPD and ab initio approaches that agreed better. Coming to the metallic distances, ab initio and EXAFS, both were able to observe the splitting of the octahedron edges and agreed on the long value (R_{Zr1b}), while they disagreed on the shorter one (R_{Zr1a}), and when averaging EXAFS data, agreement was found with XRPD (that works at higher symmetry). The octahedron diagonal (R_{Zr2}) showed good agreement between XRPD and ab initio, while EXAFS alone was able to detect the splitting of the diagonals (Figure 8c).

(vi) Experimental IR spectra were obtained upon solvent removal, progressive dehydration, and successive rehydration to compare the differences in the vibrational behavior of the two structures. Calculated spectra were also computed and used to determine unambiguously the nature of the vibrational modes through the use of animations.[101] In general, a good agreement both in position and in the intensity of the peaks was found between the two approaches. As expected, the main changes between hydroxylated and dehydroxylated forms are due to the $Zr_6O_4(OH)_4$ cluster that rearranges into a distorted Zr_6O_6 one upon activation. In particular, the band at 470 cm^{-1} due to the (HO)−Zr−(OH) bending mode disappears, and the band at 672 cm^{-1}, associated to the μ_3−O stretching, shifts to 730 cm^{-1} in case of the dehydroxylated material. IR results confirmed the high stability of the material with respect to water solvent, showing complete reversibility of the dehydration/hydration phenomenon.

(vii) A good agreement was also observed between band gaps obtained by UV−vis spectra and ab initio calculations. The materials are characterized by an absorption edge due to $\pi-\pi^*$ electronic transitions of the aromatic ring, and sample activation induces a small blue shift of the edge that moves from 4.07 to 3.94 eV (trend confirmed by the values calculated at 4.56 and 4.19 eV, respectively).

In conclusion, this work shows the necessity to combine, in an interactive and synergic way, different experimental techniques with periodic ab initio calculations to disclose and fully understand the nature of complex novel materials such as UiO-66 on structural, vibrational, and electronics grounds. None of the three adopted techniques would be able to alone disclose the hydroxylated or the dehydroxylated structure. The hydroxylated structure was solved by XRPD Rietveld analysis in the *Fm*-3*m* space group. However, because of the poor quality of the fit, this structure needed to be confirmed by EXAFS and ab initio approaches. The structure of the dehydroxylated material, obtained from a high quality Rietveld refinement (Figure 7; R_{wp} = 0.022) was unable to detect the distortion of the Zr_6O_6 octahedron (striking in the EXAFS datum, Figure 4c) and provides an input for the ab initio calculation that was not leading to a stable minimum. The lower symmetry system obtained from the ab initio calculation allowed a 3-D structure to be obtained that was used as input for a detailed EXAFS refinement. The latter evidenced a further symmetry reduction due to a significant splitting of the Zr_6O_6 octahedron diagonals.

At the moment, work is in progress to extend this approach to isoreticular versions of UiO-66 such as UiO-67 and UiO-68 and to some linker functionalized forms.

■ ASSOCIATED CONTENT

Ⓢ Supporting Information. BET nitrogen adsorption and desorption isotherms of UiO-66 at 77 K; XRPD pattern of desolvated UiO-66 after interaction with water, benzene, acetone, ethanol, DMF, ethanol, HCl, H_2O, and NaOH; CIF file for the hydroxylated structure obtained from XRPD Rietveld refinement in the *Fm*-3*m* space group; CRYSTAL input files for both structures; adopted Zirconium Basis-Set; and BET curve. This material is available free of charge via the Internet at http://pubs.acs.org.

■ AUTHOR INFORMATION

Corresponding Author

*Phone: +39011-6707841; fax: +39011-6707855; e-mail: carlo.lamberti@unito.it (C.L.). Phone: +4722855457; e-mail: k.p.lillerud@kjemi.uio.no (K.P.L.).

Present Addresses

[§]Department of Physics, Michigan Technological University, 1400 Townsend Dr., Houghton, MI 49931-1295, U.S.A.

■ ACKNOWLEDGMENT

Prof. A. Zecchina is kindly acknowledged for fruitful discussion. C. Prestipino is gratefully acknowledged for the help provided during the XAS measurements at ESRF BM29. E. Groppo, J. Vitillo, and F. Bonino are acknowledged for their contributions in understanding properties and behaviour of UiO-66. This work is a part of the STREP project MOFCAT Contract NMP4-CT-2006-033335.

■ REFERENCES

(1) Davis, M. E. *Nature* **2002**, *417*, 813–821.
(2) Yaghi, O. M.; Jernigan, R.; Li, H. L.; Davis, C. E.; Groy, T. L. *J. Chem. Soc., Dalton Trans.* **1997**, 2383–2384.
(3) Stein, A.; Melde, B. J.; Schroden, R. C. *Adv. Mater.* **2000**, *12*, 1403–1419.
(4) Ferey, G. *Chem. Mater.* **2001**, *13*, 3084–3098.
(5) James, S. L. *Chem. Soc. Rev.* **2003**, *32*, 276–288.
(6) Stein, A. *Adv. Mater.* **2003**, *15*, 763–775.

(7) Kitagawa, S.; Kitaura, R.; Noro, S. *Angew. Chem., Int. Ed.* **2004**, *43*, 2334–2375.

(8) Bordiga, S.; Lamberti, C.; Ricchiardi, G.; Regli, L.; Bonino, F.; Damin, A.; Lillerud, K. P.; Bjorgen, M.; Zecchina, A. *Chem. Commun.* **2004**, 2300–2301.

(9) Ferey, G.; Mellot-Draznieks, C.; Serre, C.; Millange, F.; Dutour, J.; Surble, S.; Margiolaki, I. *Science* **2005**, *309*, 2040–2042.

(10) Dinca, M.; Long, J. R. *J. Am. Chem. Soc.* **2007**, *129*, 11172–11176.

(11) Mulfort, K. L.; Hupp, J. T. *J. Am. Chem. Soc.* **2007**, *129*, 9604–9605.

(12) Ferey, G. *Chem. Soc. Rev.* **2008**, *37*, 191–214.

(13) Tranchemontagne, D. J.; Mendoza-Cortes, J. L.; O'Keeffe, M.; Yaghi, O. M. *Chem. Soc. Rev.* **2009**, *38*, 1257–1283.

(14) Natarajan, S.; Mahata, P. *Chem. Soc. Rev.* **2009**, *38*, 2304–2318.

(15) Wang, Z. Q.; Cohen, S. M. *Chem. Soc. Rev.* **2009**, *38*, 1315–1329.

(16) Allendorf, M. D.; Bauer, C. A.; Bhakta, R. K.; Houk, R. J. T. *Chem. Soc. Rev.* **2009**, *38*, 1330–1352.

(17) Zacher, D.; Shekhah, O.; Woll, C.; Fischer, R. A. *Chem. Soc. Rev.* **2009**, *38*, 1418–1429.

(18) Lee, J.; Farha, O. K.; Roberts, J.; Scheidt, K. A.; Nguyen, S. T.; Hupp, J. T. *Chem. Soc. Rev.* **2009**, *38*, 1450–1459.

(19) Li, J. R.; Kuppler, R. J.; Zhou, H. C. *Chem. Soc. Rev.* **2009**, *38*, 1477–1504.

(20) Dan-Hardi, M.; Serre, C.; Frot, T.; Rozes, L.; Maurin, G.; Sanchez, C.; Ferey, G. *J. Am. Chem. Soc.* **2009**, *131*, 10857–10859.

(21) Gadzikwa, T.; Farha, O. K.; Malliakas, C. D.; Kanatzidis, M. G.; Hupp, J. T.; Nguyen, S. T. *J. Am. Chem. Soc.* **2009**, *131*, 13613–13615.

(22) Shultz, A. M.; Farha, O. K.; Hupp, J. T.; Nguyen, S. T. *J. Am. Chem. Soc.* **2009**, *131*, 4204–4205.

(23) Nelson, A. P.; Farha, O. K.; Mulfort, K. L.; Hupp, J. T. *J. Am. Chem. Soc.* **2009**, *131*, 458–460.

(24) Murray, L. J.; Dinca, M.; Long, J. R. *Chem. Soc. Rev.* **2009**, *38*, 1294–1314.

(25) Demessence, A.; D'Alessandro, D. M.; Foo, M. L.; Long, J. R. *J. Am. Chem. Soc.* **2009**, *131*, 8784–8786.

(26) Farrusseng, D.; Aguado, S.; Pinel, C. *Angew. Chem., Int. Ed.* **2009**, *48*, 7502–7513.

(27) Murray, L. J.; Dinca, M.; Yano, J.; Chavan, S.; Bordiga, S.; Brown, C. M.; Long, J. R. *J. Am. Chem. Soc.* **2010**, *132*, 7856–7857.

(28) Farha, O. K.; Malliakas, C. D.; Kanatzidis, M. G.; Hupp, J. T. *J. Am. Chem. Soc.* **2010**, *132*, 950–952.

(29) Mulfort, K. L.; Farha, O. K.; Malliakas, C. D.; Kanatzidis, M. G.; Hupp, J. T. *Chem.—Eur. J.* **2010**, *16*, 276–281.

(30) Savonnet, M.; Bazer-Bachi, D.; Bats, N.; Perez-Pellitero, J.; Jeanneau, E.; Lecocq, V.; Pinel, C.; Farrusseng, D. *J. Am. Chem. Soc.* **2010**, *132*, 4518–4519.

(31) Corma, A.; Garcıa, H.; Llabres i Xamena, F. X. *Chem. Rev.* **2010**, *110*, 4606–4655.

(32) Eddaoudi, M.; Kim, J.; Rosi, N.; Vodak, D.; Wachter, J.; O'Keeffe, M.; Yaghi, O. M. *Science* **2002**, *295*, 469–472.

(33) Chui, S. S. Y.; Lo, S. M. F.; Charmant, J. P. H.; Orpen, A. G.; Williams, I. D. *Science* **1999**, *283*, 1148–1150.

(34) Li, H.; Eddaoudi, M.; O'Keeffe, M.; Yaghi, O. M. *Nature* **1999**, *402*, 276–279.

(35) Surble, S.; Serre, C.; Mellot-Draznieks, C.; Millange, F.; Ferey, G. *Chem. Commun.* **2006**, 284–286.

(36) Kickelbick, G.; Schubert, U. *Chem. Ber./Recl.* **1997**, *130*, 473–477.

(37) Kickelbick, G.; Wiede, P.; Schubert, U. *Inorg. Chim. Acta* **1999**, *284*, 1–7.

(38) Kogler, F. R.; Jupa, M.; Puchberger, M.; Schubert, U. *J. Mater. Chem.* **2004**, *14*, 3133–3138.

(39) Cavka, J. H.; Jakobsen, S.; Olsbye, U.; Guillou, N.; Lamberti, C.; Bordiga, S.; Lillerud, K. P. *J. Am. Chem. Soc.* **2008**, *130*, 13850–13851.

(40) Guillerm, V.; Gross, S.; Serre, C.; Devic, T.; Bauer, M.; Ferey, G. *Chem. Commun.* **2010**, *46*, 767–769.

(41) Ahnfeldt, T.; Guillou, N.; Gunzelmann, D.; Margiolaki, I.; Loiseau, T.; Ferey, G.; Senker, J.; Stock, N. *Angew. Chem., Int. Ed.* **2009**, *48*, 5163–5166.

(42) Lillerud, K. P.; Olsbye, U.; Tilset, M. *Top. Catal.* **2010**, *53*, 859–868.

(43) Chavan, S.; Vitillo, J. G.; Uddin, M. J.; Bonino, F.; Lamberti, C.; Groppo, E.; Lillerud, K. P.; Bordiga, S. *Chem. Mater.* **2010**, *22*, 4602–4611.

(44) Kandiah, M.; Usseglio, S.; Svelle, S.; Olsbye, U.; Lillerud, K. P.; Tilset, M. *J. Mater. Chem.* **2010**, *20*, 9848–9851.

(45) Garibay, S. J.; Cohen, S. M. *Chem. Commun.* **2010**, *46*, 7700–7702.

(46) Silva, C. G.; Luz, I.; Llabres i Xamena, F. X.; Corma, A.; Garcia, H. *Chem.—Eur. J.* **2010**, *16*, 11133–11138.

(47) Mikkelsen, J. C.; Boyce, J. B. *Phys. Rev. Lett.* **1982**, *49*, 1412–1415.

(48) Boscherini, F. In *Characterization of Semiconductor Heterostructures and Nanostructures*; Lamberti, C., Ed.; Elsevier: Amsterdam, 2008; p 289—330.

(49) Lamberti, C.; Bordiga, S.; Boscherini, F.; Pascarelli, S.; Schiavini, G. M. *Appl. Phys. Lett.* **1994**, *64*, 1430–1432.

(50) Pascarelli, S.; Boscherini, F.; Lamberti, C.; Mobilio, S. *Phys. Rev. B* **1997**, *56*, 1936–1947.

(51) Lamberti, C.; Bordiga, S.; Boscherini, F.; Mobilio, S.; Pascarelli, S.; Gastaldi, L.; Madella, M.; Papuzza, C.; Rigo, C.; Soldani, D.; Ferrari, C.; Lazzarini, L.; Salviati, G. *J. Appl. Phys.* **1998**, *83*, 1058–1077.

(52) Lamberti, C. *Surf. Sci. Rep.* **2004**, *53*, 1–197.

(53) (a) Le Toquin, R.; Paulus, W.; Cousson, A.; Prestipino, C.; Lamberti, C. *J. Am. Chem. Soc.* **2006**, *128*, 13161–13174. (b) Piovano, A.; Agostini, G.; Frenkel, A. I.; Bertier, T.; Prestipino, C.; Ceretti, M.; Paulus, W.; Lamberti, C. *J. Phys. Chem. C* **2011**, *115*, 1311–1322.

(54) Paulus, W.; Schober, H.; Eibl, S.; Johnson, M.; Berthier, T.; Hernandez, O.; Ceretti, M.; Plazanet, M.; Conder, K.; Lamberti, C. *J. Am. Chem. Soc.* **2008**, *130*, 16080–16085.

(55) Dovesi, R.; Saunders, V. R.; Roetti, R.; Orlando, R.; Zicovich-Wilson, C. M.; Pascale, F.; Civalleri, B.; Doll, K.; Harrison, N. M.; Bush, I. J.; D'Arco, P.; Llunell, M. *CRYSTAL09*; University of Torino, Torino, 2009.

(56) Dovesi, R.; Orlando, R.; Civalleri, B.; Roetti, C.; Saunders, V. R.; Zicovich-Wilson, C. M. *Z. Kristallogr.* **2005**, *220*, 571–573.

(57) Civalleri, B.; Napoli, F.; Noel, Y.; Roetti, C.; Dovesi, R. *Crystengcomm* **2006**, *8*, 364–371.

(58) (a) Coombes, D. S.; Cora, F.; Mellot-Draznieks, C.; Bell, R. G. *J. Phys. Chem. C* **2009**, *113*, 544–552. (b) Walker, A. M.; Civalleri, B.; Slater, B.; Mellot-Draznieks, C.; Cora, F.; Zicovich-Wilson, C. M.; Roman-Perez, G.; Soler, J. M.; Gale, J. D. *Angew. Chem., Int. Ed.* **2010**, *49*, 7501–7503.

(59) Valenzano, L.; Civalleri, B.; Chavan, S.; Palomino, G. T.; Arean, C. O.; Bordiga, S. *J. Phys. Chem. C* **2010**, *114*, 11185–11191.

(60) Rietveld, H. M. *Acta Crystallogr.* **1967**, *22*, 151–152.

(61) Rietveld, H. M. *J. Appl. Crystallogr.* **1969**, *2*, 65–71.

(62) Coelho, A. A. *J. Appl. Crystallogr.* **2005**, *38*, 455–461.

(63) Coelho, A. A. , 2006. http://members.optusnet.com.au/∼alancoelho/.

(64) Filipponi, A.; Borowski, M.; Bowron, D. T.; Ansell, S.; Di Cicco, A.; De Panfilis, S.; Itie, J. P. *Rev. Sci. Instrum.* **2000**, *71*, 2422–2432.

(65) (a) Lamberti, C.; Bordiga, S.; Bonino, F.; Prestipino, C.; Berlier, G.; Capello, L.; D'Acapito, F.; Llabres i Xamena, F. X.; Zecchina, A. *Phys. Chem. Chem. Phys.* **2003**, *5*, 4502–4509. (b) Lamberti, C.; Prestipino, C.; Bordiga, S.; Berlier, G.; Spoto, G.; Zecchina, A.; Laloni, A.; La Manna, F.; D'Anca, F.; Felici, R.; D'Acapito, F.; Roy, P. *Nucl. Instrum. Meth. B* **2003**, *200*, 196–201.

(66) Ravel, B.; Newville, M. *J. Synchrot. Radiat.* **2005**, *12*, 537–541.

(67) Ankudinov, A. L.; Ravel, B.; Rehr, J. J.; Conradson, S. D. *Phys. Rev. B* **1998**, *58*, 7565–7576.

(68) Becke, A. D. *J. Chem. Phys.* **1993**, *98*, 5648–5652.

(69) Lee, C.; Yang, W.; Parr, R. G. *Phys. Rev. B* **1988**, *37*, 785–789.

(70) The Zr basis set used in the calculation has been included in the Supporting Information within the CRYSTAL input files, alternatively see http://www.crystal.unito.it/Basis_Sets/zirconium.html#Zr_all_electron_dovesi_unpub.

(71) Noel, Y.; Zicovich-Wilson, C. M.; Civalleri, B.; D'Arco, P.; Dovesi, R. *Phys. Rev. B* **2002**, *65*, Art. n. 014111.

(72) Broyden, C. G. *Math. Comput.* **1965**, *19*, 577–593.

(73) Johnson, D. D. *Phys. Rev. B* **1988**, *38*, 12807–12813.

(74) Doll, K.; Saunders, V. R.; Harrison, N. M. *Int. J. Quantum Chem.* **2001**, *82*, 1–13.

(75) Doll, K. *Comput. Phys. Commun.* **2001**, *137*, 74–88.

(76) Doll, K.; Dovesi, R.; Orlando, R. *Theor. Chem. Acc.* **2004**, *112*, 394–402.

(77) Pascale, F.; Zicovich-Wilson, C. M.; López Gejo, F.; Civalleri, B.; Orlando, R.; Dovesi, R. *J. Comput. Chem.* **2004**, *25*, 888–897.

(78) Werner, P. E.; Eriksson, L.; Westdahl, M. *J. Appl. Crystallogr.* **1985**, *18*, 367–370.

(79) Altomare, A.; Giacovazzo, C.; Guagliardi, A.; Moliterni, A. G. G.; Rizzi, R.; Werner, P. E. *J. Appl. Crystallogr.* **2000**, *33*, 1180–1186.

(80) Altomare, A.; Giacovazzo, C.; Guagliardi, A.; Moliterni, A. G. G.; Rizzi, R. *J. Appl. Crystallogr.* **2000**, *33*, 1305–1310.

(81) Giacovazzo, C.; Altomare, A.; Cuocci, C.; Moliterni, A. G. G.; Rizzi, R. *J. Appl. Crystallogr.* **2002**, *35*, 422–429.

(82) Altomare, A.; Caliandro, R.; Camalli, M.; Cuocci, C.; da Silva, I.; Giacovazzo, C.; Moliterni, A. G. G.; Spagna, R. *J. Appl. Crystallogr.* **2004**, *37*, 957–966.

(83) Bordiga, S.; Roggero, I.; Ugliengo, P.; Zecchina, A.; Bolis, V.; Artioli, G.; Buzzoni, R.; Marra, G.; Rivetti, F.; Spano, G.; Lamberti, C. *J. Chem. Soc., Dalton Trans.* **2000**, 3921–3929.

(84) Bordiga, S.; Ugliengo, P.; Damin, A.; Lamberti, C.; Spoto, G.; Zecchina, A.; Spano, G.; Buzzoni, R.; Dalloro, L.; Rivetti, F. *Top. Catal.* **2001**, *15*, 43–52.

(85) Lamberti, C.; Groppo, E.; Spoto, G.; Bordiga, S.; Zecchina, A. In *Advances in Catalysis*; Elsevier Academic Press, Inc: San Diego, 2007; Vol. 51, pp 1−74.

(86) The amplitude factor is defined as $S_0^2 = |<Y_i^{N-1}||Y_f^{N-1}>|^2$, where Y_i^{N-1} and Y_f^{N-1} are the many-body wave functions of the "passive" electrons (those of the adsorbing atom that are not photoexcited) before and after excitation of the "active" electron. The value of this amplitude reduction factor should usually be between 0.7 and 0.9; however, because of the known incertitude of EXAFS in determining the exact coordination number N, its S_0^2 may result slightly greater than unit in some practical cases.

(87) In the preliminary EXAFS refinement reported in Table 1, we observe that the Zr−O distance at 2.232 Å is 6-fold degenerate. Once a more accurate model is used to refine the structure, we will realize that it corresponds to the sum of a Zr−μ3OH (degeneration = 4) and a Zr−O1 distance of the corboxylate units (degeneration = 2) that are too close to be resolved by EXAFS.

(88) Prestipino, C.; Regli, L.; Vitillo, J. G.; Bonino, F.; Damin, A.; Lamberti, C.; Zecchina, A.; Solari, P. L.; Kongshaug, K. O.; Bordiga, S. *Chem. Mater.* **2006**, *18*, 1337–1346.

(89) Szeto, K. C.; Lillerud, K. P.; Tilset, M.; Bjorgen, M.; Prestipino, C.; Zecchina, A.; Lamberti, C.; Bordiga, S. *J. Phys. Chem. B* **2006**, *110*, 21509–21520.

(90) Szeto, K. C.; Prestipino, C.; Lamberti, C.; Zecchina, A.; Bordiga, S.; Bjorgen, M.; Tilset, M.; Lillerud, K. P. *Chem. Mater.* **2007**, *19*, 211–220.

(91) Hafizovic, J.; Bjorgen, M.; Olsbye, U.; Dietzel, P. D. C.; Bordiga, S.; Prestipino, C.; Lamberti, C.; Lillerud, K. P. *J. Am. Chem. Soc.* **2007**, *129*, 3612–3620.

(92) (a) Bonino, F.; Chavan, S.; Vitillo, J. G.; Groppo, E.; Agostini, G.; Lamberti, C.; Dietzel, P. D. C.; Prestipino, C.; Bordiga, S. *Chem. Mater.* **2008**, *20*, 4957–4968. (b) Chavan, S.; Vitillo, J. G.; Groppo, E.; Bonino, F.; Lamberti, C.; Dietzel, P. D. C.; Bordiga, S. *J. Phys. Chem. C* **2009**, *113*, 3292–3299. (c) Chavan, S.; Bonino, F.; Vitillo, J. G.; Groppo, E.; Lamberti, C.; Dietzel, P. D. C.; Zecchina, A.; Bordiga, S. *Phys. Chem. Chem. Phys.* **2009**, *11*, 9811–9822.

(93) (a) Bordiga, S.; Bonino, F.; Lillerud, K. P.; Lamberti, C. *Chem. Soc. Rev.* **2010**, *39*, 4885–4927. (b) Gross, S.; Bauer, M. *Adv. Funct. Mater.* **2010**, *20*, 4026–4047.

(94) Masciocchi, N.; Galli, S.; Colombo, V.; Maspero, A.; Palmisano, G.; Seyyedi, B.; Lamberti, C.; Bordiga, S. *J. Am. Chem. Soc.* **2010**, *132*, 7902–7904.

(95) Reff is defined as one-half of the path length. For SS paths, Reff coincides consequently with the distance between the absorbing Ni and the scattering atom.

(96) The destructive interference between two or among more paths is a well known problem that can occur in some specific cases. One of the most famous cases is the almost complete disappearance of the second shell signal in both Ga and As K-edge for $In_xGa_{1-x}As$ semiconductors when x is close to 0.5. Boscherini, F.; Lamberti, C.; Pascarelli, S.; Rigo, C.; Mobilio, S. *Phys. Rev. B* **1998**, *58*, 10745–10753.

(97) Corà, F.; Alfredsson, M.; Mallia, G.; Middlemiss, D. S.; Mackrodt, W. C.; Dovesi, R.; Orlando, R. In *Principles and Applications of Density in Inorganic Chemistry II*; Springer-Verlag Berlin: Berlin, 2004; Vol. 113, pp 171−232.

(98) Riley, K. E.; Op't Holt, B. T.; Merz, K. M. *J. Chem. Theory Comput.* **2007**, *3*, 407–433.

(99) Lamberti, C.; Zecchina, A.; Groppo, E.; Bordiga, S. *Chem. Soc. Rev.* **2010**, *39*, 4951–5001.

(100) Lopez, E. F.; Escribano, V. S.; Panizza, M.; Carnasciali, M. M.; Busca, G. *J. Mater. Chem.* **2001**, *11*, 1891–1897.

(101) Animations of harmonic vibrational modes of hydroxylated and dehydroxylated UiO-66 are available at the http://www.crystal.unito.it/vibs/uio66_hydro/ and http://www.crystal.unito.it/vibs/uio66_dehydro/, Web sites respectively.

(102) Kralik, B.; Chang, E. K.; Louie, S. G. *Phys. Rev. B* **1998**, *57*, 7027–7036.

(103) Kwok, C.-K.; Aita, C. R. *J. Appl. Phys.* **1989**, *66*, 2756–2758.

(104) Muscat, J.; Wander, A.; Harrison, N. M. *Chem. Phys. Lett.* **2001**, *342*, 397–401.

(105) Harrison, N. M. *Comput. Phys. Commun.* **2001**, *137*, 59–73.

(106) Damin, A.; Xamena, F. X. L.; Lamberti, C.; Civalleri, B.; Zicovich-Wilson, C. M.; Zecchina, A. *J. Phys. Chem. B* **2004**, *108*, 1328–1336.